⊘An Extratropical Pathway for the Madden–Julian Oscillation's Influence on North Atlantic Tropical Cyclones✎

Chuan-Chieh Chang [ⓘ],[a] Sandro W. Lubis,[a] Karthik Balaguru,[a] L. Ruby Leung,[a] Samson M. Hagos,[a] and Philip J. Klotzbach[b]

[a] *Pacific Northwest National Laboratory, Richland, Washington*
[b] *Department of Atmospheric Science, Colorado State University, Fort Collins, Colorado*

ABSTRACT: This study investigates the combined impacts of the Madden–Julian oscillation (MJO) and extratropical anticyclonic Rossby wave breaking (AWB) on subseasonal Atlantic tropical cyclone (TC) activity and their physical connections. Our results show that during MJO phases 2–3 (enhanced Indian Ocean convection) and 6–7 (enhanced tropical Pacific convection), there are significant changes in basinwide TC activity. The MJO and AWB collaborate to suppress basinwide TC activity during phases 6–7 but not during phases 2–3. During phases 6–7, when AWB occurs, various TC metrics including hurricanes, accumulated cyclone energy, and rapid intensification probability decrease by ~50%–80%. Simultaneously, large-scale environmental variables, like vertical wind shear, precipitable water, and sea surface temperatures become extremely unfavorable for TC formation and intensification, compared to periods characterized by suppressed AWB activity during the same MJO phases. Further investigation reveals that AWB events during phases 6–7 occur in concert with the development of a stronger anticyclone in the lower troposphere, which transports more dry, stable extratropical air equatorward, and drives enhanced tropical SST cooling. As a result, individual AWB events in phases 6–7 can disturb the development of surrounding TCs to a greater extent than their phases 2–3 counterparts. The influence of the MJO on AWB over the western subtropical Atlantic can be attributed to the modulation of the convectively forced Rossby wave source over the tropical eastern Pacific. A significant number of Rossby waves initiating from this region during phases 5–6 propagate into the subtropical North Atlantic, preceding the occurrence of AWB events in phases 6–7.

KEYWORDS: Madden-Julian oscillation; Rossby waves; Wave breaking; Tropical cyclones

1. Introduction and objectives

Tropical cyclones (TCs) are one of the most severe storm systems on Earth. The torrential rain, storm surges, and strong winds they produce upon landfall cause property damage and loss of life in coastal regions. Skillful predictions of TC activity on subseasonal time scales (7–60 days) can aid storm preparedness and mitigate their destructive impacts (Brunet et al. 2010). As the dominant component of intraseasonal (30–90 days) variability in the tropical atmosphere, the Madden–Julian oscillation (MJO; Madden and Julian 1972; Xie et al. 1963) has been widely recognized to modulate subseasonal TC activity over various oceanic regions (Camargo et al. 2009; Klotzbach 2014; Klotzbach and Oliver 2015a). The large-scale atmospheric circulation and convective signals of the MJO propagate eastward at an average speed of ~5 m s^{-1} across the Indian and western Pacific Oceans (Madden and Julian 1972; Zhang 2005). Meanwhile, the MJO perturbs the

underlying upper ocean through fluxes of momentum, turbulent heat, and radiation (Balaguru et al. 2021; Hendon and Glick 1997; Krishnamurti et al. 1988; Lau and Sui 1997; Zhang 1996).

Following the convectively active regions associated with the MJO, the areas with the highest TC track density are observed to shift eastward from the Indian Ocean to the eastern Pacific (Camargo et al. 2009; Klotzbach 2014; Klotzbach and Oliver 2015a; Zhang 2013). The convective phase, or the active phase of the MJO promotes tropical cyclogenesis and storm development by reducing vertical wind shear (VWS), moistening the middle troposphere, and enhancing low-level relative vorticity and convergence (Aiyyer and Molinari 2008; Camargo et al. 2009; Frank and Roundy 2006; Klotzbach 2014; Liebmann et al. 1994; Maloney and Hartmann 2000; Maloney and Shaman 2008; Mo 2000). Owing to the strong contemporaneous relationship between TC activity and the MJO in various basins, the phase and amplitude of MJO are commonly used as predictors in subseasonal statistical models (Henderson and Maloney 2013; Leroy and Wheeler 2008). An accurate representation of the MJO's evolution, and the ability to simulate its interaction with TCs, are generally regarded as key ingredients for skillful prediction of basin-scale TC occurrence beyond 2 weeks in dynamical forecast systems (Camp et al. 2018; Jiang et al. 2018; Lee et al. 2018; Li et al. 2016; Li et al. 2022; Vitart 2009; Vitart et al. 2010).

The pronounced influence of the MJO on Atlantic TCs, especially for storms forming over the main development region (MDR; Goldenberg et al. 2001), has been extensively investigated

---

Corresponding author: Chuan-Chieh Chang, jay.chang@pnnl.gov

(Barrett and Leslie 2009; Klotzbach 2010, 2012; Klotzbach and Oliver 2015b; Klotzbach et al. 2023; Maloney and Shaman 2008; Mo 2000; Ventrice et al. 2011). When the convective signal of the MJO is over Africa and the Indian Ocean (i.e., phases 1–3 of the real-time multivariate MJO (RMM) index; Wheeler and Hendon 2004), TC activity over the tropical North Atlantic becomes more active (Klotzbach 2010, 2012; Klotzbach and Oliver 2015b). Conversely, when the MJO is in phases 5–7 indicating enhanced convection over the tropical Pacific, Atlantic TC activity is typically reduced (Klotzbach 2010, 2012; Klotzbach and Oliver 2015b; Mo 2000).

As documented by Mo (2000), when the convective signal of the MJO is over the Indian Ocean, in conjunction with suppressed convection over the Pacific, positive 200-hPa streamfunction anomalies occur in the tropical North Atlantic. The corresponding upper-tropospheric easterly wind anomalies oppose the climatological westerlies, thus reducing VWS over the MDR. Simultaneously, the strengthening of low-level westerlies near the West African coast enhances cyclonic shear on the equatorward side of the African easterly jet (Ventrice et al. 2011). Consequently, variations in the horizontal shear facilitate barotropic energy conversions from the mean state to the eddies (Charney and Stern 1962; Fjortoft 1950), resulting in anomalously vigorous African easterly waves (AEWs) (Alaka and Maloney 2012; Maloney and Shaman 2008; Ventrice et al. 2011), suggestive of more frequent and stronger seeding for TCs (Hopsch et al. 2007; Thorncroft and Hodges 2001). In contrast, AEW activity weakens as the MJO propagates toward the western Pacific. Amplified intraseasonal convection over the central-to-eastern Pacific is typically linked to negative anomalies of eddy kinetic energy (EKE) and significantly enhanced VWS over the tropical North Atlantic (Maloney and Shaman 2008; Mo 2000; Ventrice et al. 2011).

The MJO's control of TCs largely resides in its ability to modulate various environmental conditions (Camargo et al. 2009; Klotzbach 2010, 2012; Klotzbach et al. 2023; Klotzbach and Oliver 2015b; Mo 2000) and preexisting tropical synoptic disturbances (Aiyyer and Molinari 2008; Maloney and Shaman 2008; Ventrice et al. 2011). However, subseasonal Atlantic TC variability cannot be fully explained by the MJO (Hansen et al. 2020). Characterized by irreversible overturning of potential vorticity (PV) on isentropic surfaces, Rossby wave breaking (RWB) occurs when westerly wind speeds are comparable to wave phase speeds (McIntyre and Palmer 1983; Randel and Held 1991). RWB is acknowledged as an important contributor in mixing momentum (Randel and Held 1991) and moisture (Waugh 2005) between the extratropics and tropics. As suggested by Thorncroft et al. (1993), occurrence of RWB denotes the late stage of a baroclinic wave's life cycle and can be segregated into two types based on the behavior of the upper-tropospheric trough: anticyclonic wave breaking (AWB) and cyclonic wave breaking (CWB). AWB features backward-tilted, progressively thinning troughs being advected anticyclonically and equatorward, preferentially occurring on the equatorward side of the westerly jet. CWB, by contrast, is dominated by a broadening trough wrapping itself up cyclonically and is mostly seen on the poleward flank of the jet, where horizontal cyclonic shear dominates.

Although both CWB and AWB events have been suggested to affect the evolution of a TC, including its genesis, track, and changes in intensity (Davis and Bosart 2004; Hanley et al. 2001; Manganello et al. 2019; Zhang et al. 2016, 2017), the relationship between warm-season AWB and Atlantic TCs has become a subject of intense research during the past few years (Bentley et al. 2017; Galarneau et al. 2015; Li et al. 2018; Papin et al. 2020, 2023; Zhang et al. 2016, 2017). AWB has been suggested to occasionally trigger TC genesis (Bentley et al. 2017; Davis and Bosart 2004; Galarneau et al. 2015) through decreased static stability and enhanced upward motion along the leading edge of the trough (Funatsu and Waugh 2008; Kiladis and Weickmann 1992; Kiladis 1998). Recurrent AWB events, however, drive significant large-scale anomalies and lead to suppression of Atlantic TC activity on seasonal time scales (Chang and Wang 2018; Jones et al. 2020; Papin et al. 2020; Zhang et al. 2016, 2017).

The tightened PV gradient on the southern side of the trough intensifies upper-level westerly winds, thereby enhancing VWS over the Atlantic MDR (Papin et al. 2023; Zhang et al. 2016, 2017). Moreover, relative humidity decreases within the high-PV tongue, owing to the intrusion of stable dry air from the lower stratosphere (Waugh 2005). Meanwhile, subsidence within the PV streamer supports a divergent near-surface anticyclone, promoting negative SST anomalies in the MDR by organizing patterns of turbulent heat flux at the air–sea interface (Strong and Magnusdottir 2009; Zhang and Wang 2019). Since AWB affects both dynamic and thermodynamic states on synoptic scales, forecast errors in AWB degrade a model's skill in capturing variations of weekly TC activity (Li et al. 2018) and could be an important source for mean state biases in subseasonal prediction systems (Papin et al. 2023).

Previous studies showed that the locations and timing of AWB events in the cold season are influenced by the MJO through its impacts on subtropical and extratropical jets (Cassou 2008; MacRitchie and Roundy 2016; Moore et al. 2010). AWB occurs significantly more frequently in the central and eastern Pacific when MJO convection is present in the Maritime Continent and the eastern Indian Ocean (MacRitchie and Roundy 2016; Moore et al. 2010). During this time, the North Pacific jet retracts westward and shifts to the north, making the background mean flow unable to sustain linear wave propagation near the jet exit regions (Moore et al. 2010). The opposite is true when the convective signal of the MJO migrates to east of the date line (Moore et al. 2010). MacRitchie and Roundy (2016) further suggested a two-way interaction between the MJO and AWB. The cutoff low resulting from AWB intensifies upper-level westerly winds ahead of the MJO's convection and acts to enhance intraseasonal convection associated with the MJO as it propagates eastward. Over the North Atlantic, previous studies (Cassou 2008; Benedict et al. 2004; Woollings et al. 2008) suggested that the probability of a positive phase of the North Atlantic Oscillation (NAO) significantly increases in response to MJO-associated heating over the

Indian Ocean, with enhanced AWB activity serving as the key catalyst for the development of positive NAO regime.

In contrast to the relatively well-established MJO–AWB connection in winter, the possible role of the MJO in modulating the spatiotemporal distribution of warm-season AWB has received limited attention. A recent study by Li et al. (2018) explored the link between summertime AWB and the MJO and found that the likelihood of wave breaking is reduced in phases 2–3 but enhanced in phases 6–7 over the subtropical to tropical west Atlantic. However, the dynamical mechanism behind this link is largely unclear. Moreover, they showed that the occurrence of AWB does not always lead to suppressed Atlantic TC activity on subseasonal time scales, likely due to the modulation of TCs by the MJO. Hence, the full spectrum of AWB–MJO interactions on Atlantic TC activity remains to be explored. In this study, we revisit how various large-scale environmental conditions, Atlantic TC activity, and the statistics of AWB are modulated by the MJO. Then, we seek to address the following questions:

1) How do the impacts of AWB on Atlantic TCs evolve with different phases of the MJO?
2) What are the plausible physical connections between summertime AWB and the MJO?

The rest of this paper is organized as follows. Section 2 describes the data and methodology. Changes in different environmental parameters, AWB statistics, and Atlantic TC activity, along with the first question, are investigated in section 3. Section 4 addresses the possible physical mechanisms between AWB and the MJO, followed by a summary and discussion in section 5.

2. Data and methods

a. Data

Consistent with previous studies, the phase and amplitude of the MJO are determined using the real-time multivariate MJO index (RMM; Wheeler and Hendon 2004). The indices are available from 1 June 1974 to present, except for 1978 when outgoing longwave radiation (OLR) data were unavailable. To detect AWB events and examine variations of the large-scale environment, we use data from the Japanese 55-yr Reanalysis dataset (JRA-55; Kobayashi et al. 2015). Six-hourly atmospheric fields on both isobaric and isentropic surfaces, along with sea surface temperatures (SSTs), are available on a $1.25° \times 1.25°$ grid from 1958 to the near-present. We focus on the North Atlantic hurricane season, June–November, from 1974 to 2021. Daily-averaged National Oceanic and Atmospheric Administration satellite OLR (Liebmann and Smith 1996) data with a horizontal resolution of $2.5° \times 2.5°$ are used as a proxy for tropical convection.

Six-hourly TC track and intensity data for the period of 1974–2021 are obtained from the Atlantic hurricane database (HURDAT2; Landsea and Franklin 2013). Various TC metrics analyzed in this study include named storms (NS), named storm days (NSD), hurricanes (H), hurricane days (HD), major hurricanes (MH), major hurricane days (MHD), accumulated cyclone energy (ACE), and rapid intensification probability (RI probability). Definitions of NS, NSD, H, HD, MH, and MHD are listed in Klotzbach and Gray (2003), and ACE is calculated as in Bell et al. (2000). We define an RI event when a TC with an initial wind speed of $\geq$34 kt (1 kt $\approx$ 0.51 m s^{-1}) experiences an intensification $\geq$30 kt within 24 h (Kaplan and DeMaria 2003). Following Klotzbach (2014), here we compute the percentage probability of a TC experiencing at least one RI event during its lifetime. Also, subtropical cyclones, which exhibit characteristics of both tropical and extratropical cyclones (OFCM 2023, p. N-6), are excluded from our analyses. The reason for this exclusion is that the impacts of the MJO on these types of storms are likely limited (Klotzbach 2010).

In the following analyses, composite TC activity and anomalies of different environmental variables are calculated for different phases of the MJO when the RMM index amplitude exceeds 1 to exclude periods when the MJO is weak. The total number of days used to construct the composites is 5000 (~58% of days during the hurricane season). Daily anomalies are defined as the departures from the seasonal cycle. The seasonal cycles for all fields are constructed by first calculating the long-term (1974–2021) daily mean for each calendar day, and then a 7-day running-mean filter is further applied to the long-term daily mean data to remove the remaining high-frequency fluctuations.

b. AWB detection

To identify AWB events, 6-hourly PV fields on the 350-K isentropic surface are fed into an automatic detection algorithm (Abatzoglou and Magnusdottir 2006; Strong and Magnusdottir 2008; Zhang et al. 2016, 2017), which searches for the circumglobal PV contours crossing a meridian more than once. The time, centroid location, area, and meridional and zonal boundaries of the equatorward-intruding high-PV tongue are recorded by the algorithm every 6 h. In this study, the influence of wave breaking is calculated by the areal fraction of AWB (hereafter AWB_area; see schematic shown in Fig. A1 in the appendix). Here we define domain A, which is determined by the zonal and meridional boundaries of the high-PV tongue, as the region affected by the AWB (Fig. A1). Since the algorithm records the 6-hourly area of the high-PV tongue (see the yellow shading in Fig. A1), we can calculate the AWB_area over domain A. We estimate the areal ratio covered by high-PV air over a certain domain instead of directly counting the grid points embedded within the PV streamer, because the grid points are not explicitly recorded by the algorithm at each time step. The AWB_area is a comprehensive measure of AWB activity, as it considers AWB location, frequency, and geographical extent.

c. Rossby wave ray tracing

Wave breaking events are often preceded by an upstream Rossby wave train that extends from the North Pacific (Postel and Hitchman 2001; Zavadoff and Kirtman 2019, 2021; Zhang and Wang 2018). To better understand the paths of Rossby wave propagation, we implement a wave ray tracing technique, developed by Li et al. (2015) and Zhao et al. (2015).

In this ray-tracing algorithm, a two-dimensional wave dispersion relationship is applied by considering the effect of the meridional basic wind on a beta plane. The dispersion relationship for a horizontally nonuniform flow can be written as (Karoly 1983)

$$\omega = \overline{u}_M k + \overline{v}_M l + \frac{\overline{q}_x l - \overline{q}_y k}{k^2 + l^2}, \tag{1}$$

where ω, k, l, $\overline{u}_M$, and $\overline{v}_M$ are the angular frequency, zonal wavenumber, meridional wavenumber, basic-state zonal, and meridional flows, respectively. In these expressions, the overbars denote a time mean. Following the definition given by Postel and Hitchman (2001), the basic state is defined as the 200-hPa horizontal winds averaged over the period of 31 days prior to major AWB events (see section 4 for the definition of "major AWB events"). A spectral triangular truncation at wavenumber 11 is further used to smooth the background flow. The variables $\overline{q}_x$ and $\overline{q}_y$ denote the zonal and meridional gradients of absolute vorticity, respectively. Note that we focus on traveling waves in this study, and therefore the nonzero angular frequency is expressed as $\omega = C_x k / R_E$, where C_x and R_E denote the wave's phase speed and Earth's radius, respectively. Once we know the initial zonal wavenumber and angular frequency, the initial meridional wavenumber can be obtained by solving Eq. (1). The zonal and meridional components of group velocity can be expressed as

$$\frac{d_g x}{dt} = u_g = \overline{u}_M + \frac{(k^2 - l^2)\overline{q}_y - 2kl\overline{q}_x}{K^4} \quad \text{and} \tag{2}$$

$$\frac{d_g y}{dt} = v_g = \overline{v}_M + \frac{(k^2 - l^2)\overline{q}_x + 2kl\overline{q}_y}{K^4}, \tag{3}$$

where K^2 is the total wavenumber, which is expressed by $K^2 = \overline{q}_y k - \overline{q}_x l / (\overline{u}_M k + \overline{v}_M l - \omega)$; and $d_g/dt = \partial/\partial t + u_g(\partial/\partial x) + v_g(\partial/\partial y)$ represents the Lagrangian variation moving at the group velocity, with x and y being the longitude and latitude of rays at time t. Given the initial location of the ray, its displacement with time is computed by the fourth-order Runge–Kutta method (Press et al. 1992) and is integrated for 10 days.

d. Statistical significance

If not specified otherwise, a two-sample Welch's test is used to determine whether composite differences in various environmental parameters and AWB activity are significant at the 95% confidence level. Before calculating the p values, the degrees of freedom (v) in Welch's t test can be expressed using the formula (Moser and Stevens 1992)

$$v = \frac{\left(\dfrac{s_1^2}{N_1} + \dfrac{s_2^2}{N_2}\right)^2}{\dfrac{s_1^4}{N_1^2 v_1} + \dfrac{s_2^4}{N_2^2 v_2}}.$$

Here, N_i represents the sample size, s_i represents the sample standard deviation, and v_i denotes the degrees of freedom for sample i. Treating each day of data as an independent sample

may lead to an overestimation of degrees of freedom when multiple days belong to a single MJO event. Wheeler and Hendon (2004) have documented that the typical duration of the MJO in a specific phase is approximately 5 days. Thus, following the approach taken by Alaka and Maloney (2012), the degrees of freedom are calculated by dividing both the number of days in the MJO phases and the climatological daily means by 5.

To better address whether a TC index in a certain MJO phase is statistically different from the mean of all MJO phases, a Monte Carlo bootstrap resampling method is used, as in Klotzbach (2014). For example, if one is interested in knowing whether the number of TCs observed in phase 2 is significantly higher (or lower) than the mean of all phases, and 50 TCs were observed to form during the 500-day periods of phase 2. We first calculate the number of TCs that formed in 500 days randomly chosen from the full time series when the MJO amplitude is greater than 1 (i.e., 5000 days). This process is repeated 10 000 times. The obtained results are then sorted to extract the 500th, 1000th, 9000th, and 9500th values, representing the 5%, 10%, 90%, and 95% confidence intervals. Next, statistical significance is denoted if the observed TC frequency in phase 2 passes the bootstrap resampling test. The same statistical test is applied for all TC indices and in each MJO phase.

3. Combined influences of the MJO and AWB on Atlantic TC activity

a. Modulation of Atlantic TC activity and associated large-scale conditions by the MJO

We first revisit the impact of the MJO on Atlantic TC activity. Compared with previous studies (Klotzbach 2010, 2012, 2014; Klotzbach and Oliver 2015b), our analysis includes an additional ~10 years of data and extends these earlier findings to the near present. For simplicity, the eight MJO phases are divided into four groups based on the approximate locations of enhanced MJO convection, and normalized TC activity during different groups of the MJO is tabulated in Table 1. Following previous studies (Klotzbach 2010, 2012, 2014), each TC's statistics are counted for the MJO phase at the time when the TC formed. For instance, if a TC formed in phase 2 and subsequently intensified into a major hurricane in phase 4, it would be classified as a major hurricane for phase 2. As seen in Table 1, significant changes are evident for different TC metrics, particularly for phases 2–3 and phases 6–7. Phases 2–3 are characterized by largely enhanced basinwide TC activity, whereas all TC indices are significantly reduced during phases 6–7. Relative to phases 6–7, several measures of TC activity, including storm number, hurricanes, major hurricanes, named storm days, and ACE increase more than 100% in phases 2–3. Hurricane days and major hurricane days show even stronger responses. During MJO phases 2–3, major hurricane days, and hurricane days occur 4 and 3 times more often, respectively, than in phases 6 and 7. Nevertheless, the odds of a storm undergoing at least one RI episode during its lifetime do not exhibit a significant change during phases 2–3. A plausible explanation is that storms forming in phases 2–3 may encounter a less favorable environment in phases 4–5 as they approach the coast

TABLE 1. Normalized values for different TC metrics, including named storms (NS), hurricanes (H), major hurricanes (MH), named storm days (NSD), hurricane days (HD), major hurricane days (MHD), ACE, and RI probability. These values represent the level of TC activity that is expected for 100 days during a specific MJO category and are generated by TCs forming during 1974–2021 when the amplitude of the RMM index is greater than 1. Positive differences from the phase 1–8 average that are significant at the 95% (90%) confidence level are in boldface with (without) an asterisk, while negative differences from the phase 1–8 average that are significant at the 95% (90%) confidence level are in italic with (without) an asterisk.

	MJO phases			
	2 + 3 (122 TCs)	4 + 5 (84 TCs)	6 + 7 (46 TCs)	8 + 1 (87 TCs)
No. of days	1296	1368	996	1340
NS	**9.4***	6.1	*4.6**	6.5
H	**5.2***	3.7	*2.5**	3.3
MH	**2.4***	1.5	*0.9**	1.3
NSD	**47.7***	29.4	*21.5**	31.7
HD	**23.7***	16.0	*7.8**	17.1
MHD	**4.5**	3.0	*0.98**	3.9
ACE	**82.9***	53.9	*31.9**	61.2
RI probability	33.6%	36.9%	*28.2%*	35.6%

(not shown). The other MJO phase pairs do not show significant differences for various TC indices compared to the average of phases 1–8.

The significant contrast in basinwide TC activity between phases 2–3 and phases 6–7 prompts us to next examine anomalies in large-scale environmental conditions. Variations in the VWS (defined as the magnitude of the vector wind difference between 200 and 850 hPa), total precipitable water (TPW), and SST associated with different phases of the MJO are shown in Fig. 1. During phases 2–3, VWS decreases over large swaths of the MDR, with the strongest negative anomalies in the Caribbean, while a broad region north of the Bahamas is characterized by higher VWS (Fig. 1a). Significant positive anomalies in TPW develop over the MDR and the Gulf of Mexico (Fig. 1b), possibly due to reduced extratropical dry air intrusion associated with the decreasing occurrence of AWBs (Fig. 2a). Simultaneously, following enhanced convection over the Indian Ocean, anomalous low-level westerly winds (Fig. 1c) tend to oppose the climatological easterly trades. These anomalies create perturbations in local turbulent heat fluxes (not shown), reducing the heat uptake from the tropical Atlantic Ocean. In addition to fluctuations in SST, tropospheric moisture, and VWS, AEW activity is found to vary in a manner consistent with what was reported in previous studies (Fig. S1 in the online supplemental material; Aiyyer and Molinari 2008; Ventrice et al. 2011). Changes in 2.5–9-day-filtered EKE show positive anomalies prevailing near the coast of West Africa, the western MDR, and the Gulf of Mexico (Fig. S1). Taken together, an anomalously moist troposphere, warmer-than-normal SSTs, reduced VWS, and enhanced AEW activity, constitute favorable conditions for TC genesis and development south of 30°N during phases 2–3.

As the convective signal of the MJO continues to propagate toward the International Date Line (i.e., phases 6–7), the spatial patterns of composite anomalies (Figs. 1d–f) are almost the mirror image of those observed in phases 2–3 (Figs. 1a–c). An increase in VWS (Fig. 1d) and significantly reduced TPW (Fig. 1e), along with cooler-than-normal SSTs (Fig. 1f) south of 30°N, discourage TC development and are consistent with

suppressed basinwide TC activity (Table 1). It is also worth noting that the SST anomalies exhibit relatively low amplitudes (Figs. 1c–f). In contrast, the difference in VWS across various phases can reach approximately 4–5 m s^{-1} over the MDR (Figs. 1a,b), serving as a major pathway for the MJO's influence on Atlantic TCs (Hansen et al. 2020; Klotzbach 2010).

b. Variations in AWB activity

The above results confirm the critical role of the MJO in driving Atlantic TC activity changes on subseasonal time scales and are generally in good agreement with previous findings (Klotzbach 2010, 2012; Klotzbach and Oliver 2015b; Ventrice et al. 2011). In the analysis that follows, we explore how the statistics of breaking waves vary with respect to different MJO phases. The long-term (1974–2021) climatology (black contours) and changes in AWB_area (shading) are shown in Figs. 2a and 2b. Regions experiencing frequent occurrences of AWB are located southeast of the westerly jet, where the upper-tropospheric flow is diffluent, and the waveguide is relatively weak (Abatzoglou and Magnusdottir 2006; Postel and Hitchman 1999). The occurrence probability of AWB is significantly reduced over the Gulf of Mexico and the western part of the subtropical Atlantic, but AWB activity is slightly enhanced over the eastern MDR in phases 2–3 (Fig. 2a). By contrast, during phases 6–7, a broad region extending from the northeastern coast of the United States to Cuba is characterized by positive anomalies of AWB_area, accompanied by a small decrease in AWB activity over the central-to-eastern MDR (Fig. 2b).

To better understand how the MJO is linked to variations of AWB activity on daily time scales, we construct probability distribution functions (PDFs) of anomalous AWB_area with respect to different MJO phases (Fig. 2c). Before constructing the PDFs, the long-term daily climatology of AWB_area is first removed, and then daily anomalies are averaged over the western subtropical North Atlantic (20°–35°N, 85°–45°W; the dashed purple domains in Figs. 2a,b), where the subseasonal variability of AWB is the largest (Li et al. 2018). Moreover,
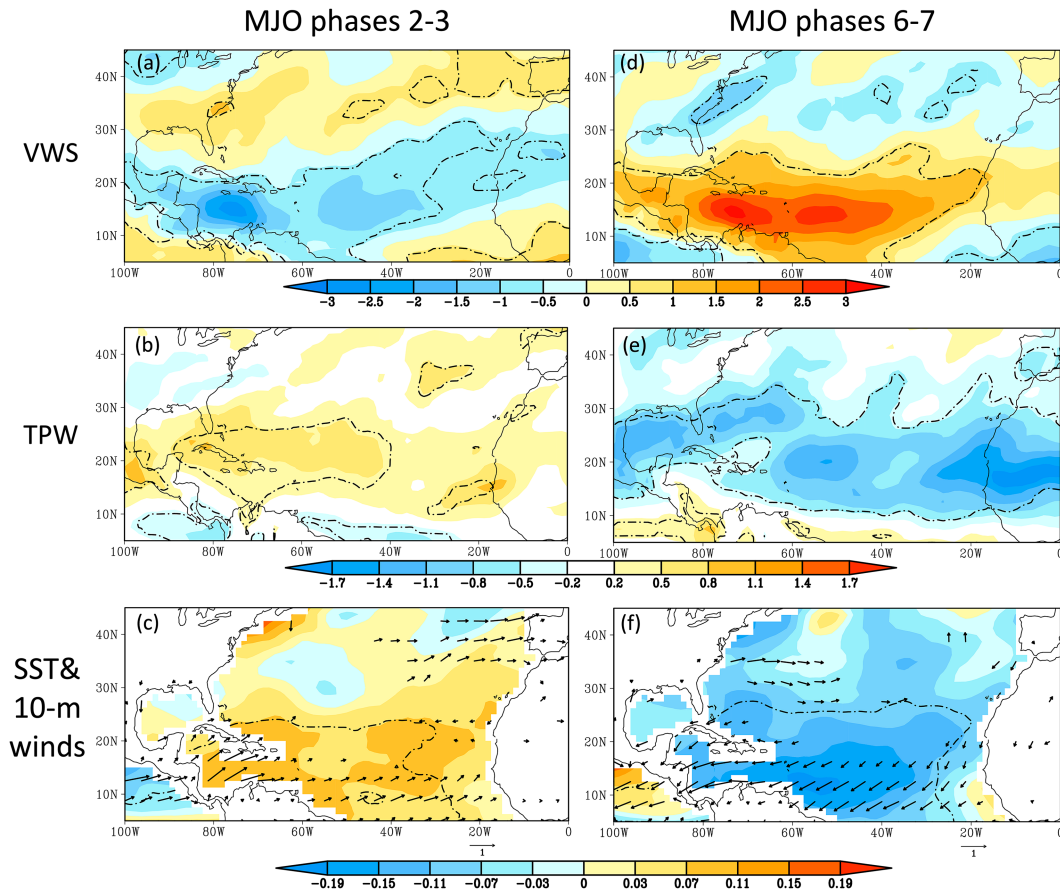
MJO phases 2-3　　　　　　　　　　　　MJO phases 6-7

FIG. 1. Anomalies in (a) VWS (m s^{-1}), (b) TPW (kg m^{-2}), and (c) SST (K) during phases 2–3. Black dashed lines highlight regions significant at the 95% confidence level. Also, vectors in (c) are anomalous 10-m winds (m s^{-1}) in phases 2 and 3, and only differences exceeding the 95% confidence level are shown. (d)–(f) As in (a)–(c), but for RMM phases 6–7.

the occurrence of AWB over this region exerts the strongest negative influence on basinwide TC activity (Zhang et al. 2017). Relative to phases 2–3, the significant rightward shift in domain-averaged anomalous AWB_area during phases 6–7 (Fig. 2c) suggests an increasing preference for extratropical waves to penetrate the western part of the subtropical Atlantic when the convective signal of the MJO is maximized over the central to eastern Pacific. The anomaly of the AWB_area, averaged over the subtropical western Atlantic during phases 2 and 3 is −1.25%. During phases 6 and 7, the anomaly increases to +1.05%. This difference is statistically significant at a 99% confidence level. The relationship between the AWB and MJO is robust even when highly amplified ENSO and Atlantic meridional mode (AMM; Chiang and Vimont 2004) years are removed (Fig. S2). Both ENSO and the AMM have been shown to strongly affect the seasonal frequency of AWB occurrence (Abatzoglou and Magnusdottir 2006; Waugh and Polvani 2000; Zhang and Wang 2019). In addition, since AWB is associated with significant atmospheric synoptic variability (Li et al. 2018; Zhang et al. 2017) and can cause fluctuations in tropical

SST (Strong and Magnusdottir 2009; Zhang and Wang 2019), the difference in the probability of AWB occurrence partially explains why both thermodynamic and dynamic environments are more favorable for TC intensification and genesis during phases 2–3, but tend to inhibit the convective development of TCs in phases 6–7 (Fig. 1 and Table 1). Our results are also consistent with Li et al. (2018), who first documented the AWB–MJO link in the warm season.

c. Impacts of nonlinear MJO–AWB interaction on subseasonal Atlantic TC activity

The occurrence probability of AWB varies significantly across different MJO phases over the northwestern Atlantic. However, for both phases 2–3 and phases 6–7, the standard deviations of the spatially averaged AWB_area anomalies are large (>10%, Fig. 2c). This indicates that the spatial extent of the equatorward-intruding high-PV tongue undergoes substantial changes from day to day, even within the same MJO phase. Given that AWB can occur throughout the MJO's life cycle, it is crucial to understand how the negative impacts of AWB on Atlantic TCs evolve during different MJO phases.
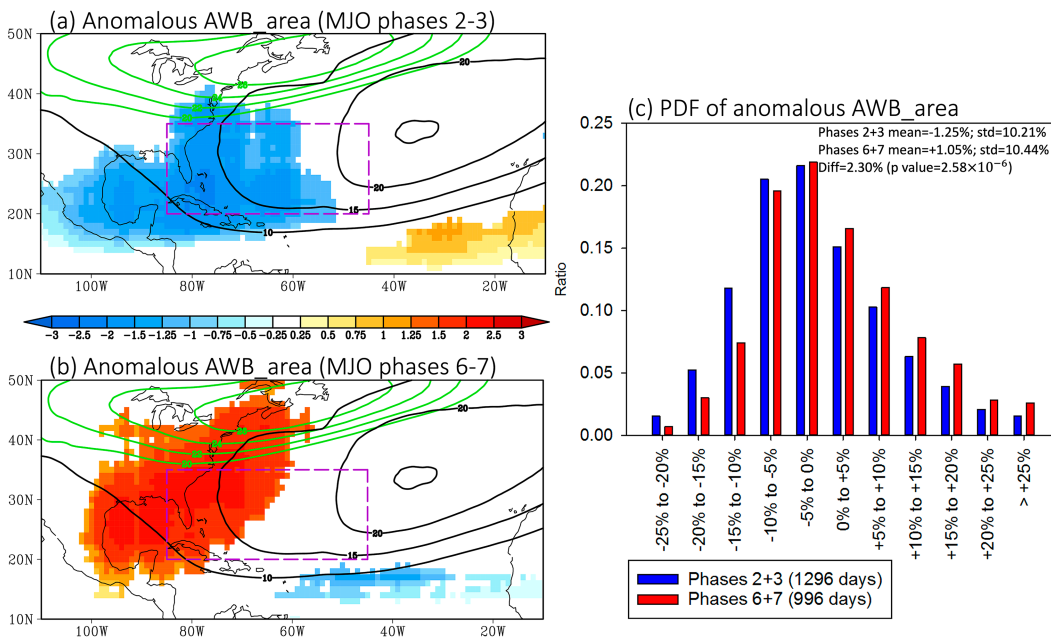
FIG. 2. Climatological seasonal-mean 200-hPa zonal wind (m s^{-1}; green contours), AWB_area (%; black contours), and changes in AWB_area (%; shaded) relative to the long-term daily climatology for (a) phases 2–3 and (b) phases 6–7. Only differences exceeding the 95% confidence level are shown. (c) Probability distributions of daily anomalous AWB_area averaged over the subtropical western Atlantic [20°–35°N, 85°–45°W; dashed purple domains in (a) and (b)] for phases 2–3 (blue bars) and phases 6–7 (red bars).

To explore the response of TCs to the presence of AWB during various MJO phases, we first separate the days during phases 2–3 into two groups. This classification is based on whether the spatially averaged anomaly of AWB_area over the western subtropical North Atlantic (20°–35°N, 85°–45°W) is positive or negative, denoted as AWB_area (+) and AWB_area (−), respectively. The positive (negative) anomaly of AWB_area clearly identifies the presence (absence) of

the reversed meridional PV gradient along the tropopause (Fig. S3). We then classify each TC based on the AWB_area anomaly at the time of its formation. The statistics for different TC metrics are presented in Table 2. Similar analyses are done for phases 6–7. Wave breakings result in a modest reduction of major hurricanes during phases 2–3 (Table 2). When compared to the AWB_area (−), the number of major hurricanes decreases by ~37% in the AWB_area (+). Major hurricane days

TABLE 2. Normalized values of different TC metrics in both the AWB_area (+) and AWB_area (−) during MJO phases 2–3 or phases 6–7. For the values listed in the first two columns, positive differences from the phase 2–3 average that are statistically significant at the 95% (90%) confidence level are in boldface with (without) an asterisk, while negative differences from the phase 2–3 average that are statistically significant at the 95% (90%) confidence level are in italic with (without) an asterisk. Statistical significance is determined using a Monte Carlo bootstrap resampling method. The same demarcations are applied to the values listed in the two columns on the right-hand side, but for the phase 6–7 average.

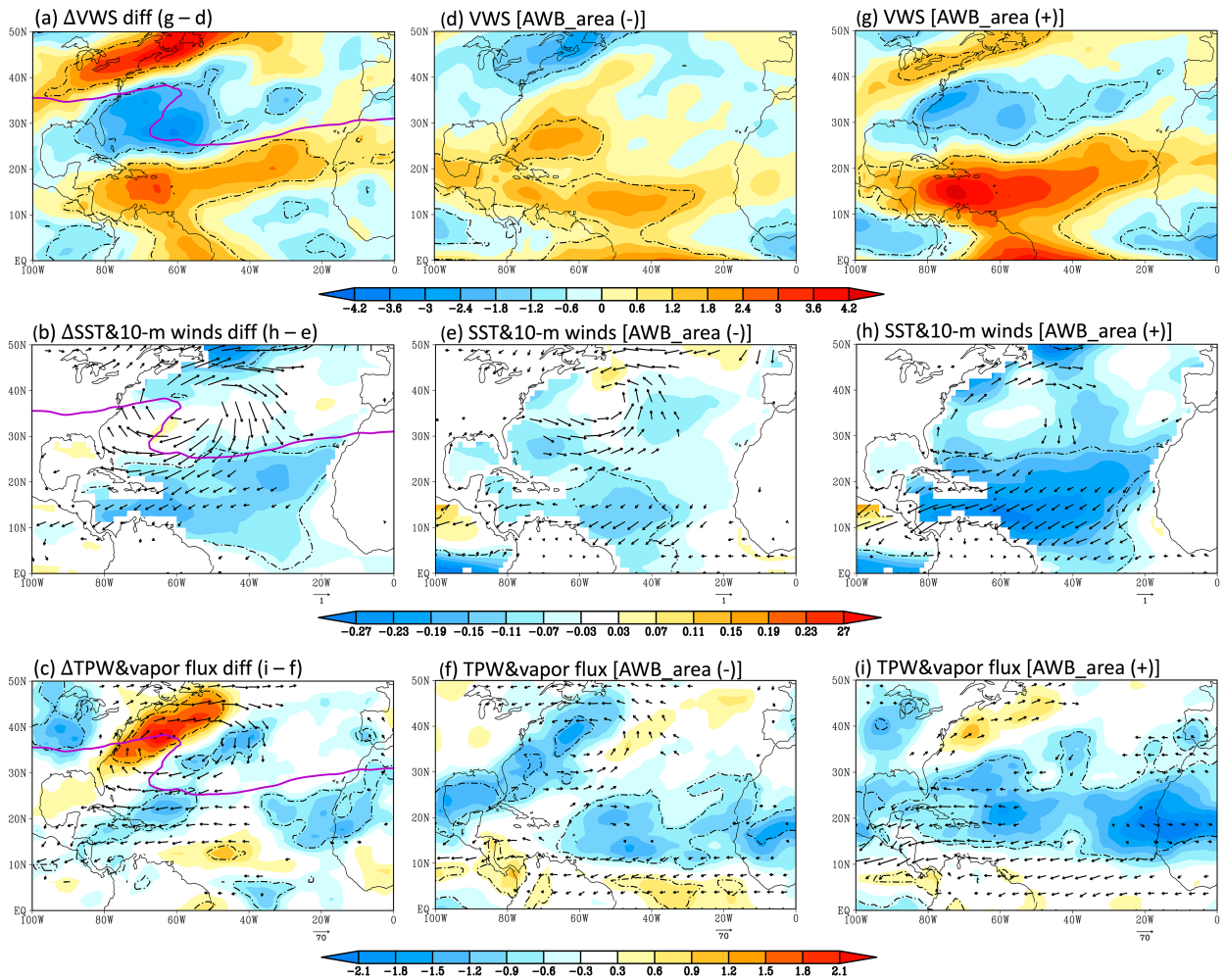|	MJO phases			
	2 + 3		6 + 7	
	AWB_area (+) (509 days; 49 TCs)	AWB_area (−) (787 days; 73 TCs)	AWB_area (+) (472 days; 14 TCs)	AWB_area (−) (524 days; 32 TCs)
NS	9.6	9.3	*3.0**	**6.1***
H	5.3	5.1	*1.5**	**3.4***
MH	*1.8*	**2.8**	*0.4**	**1.3***
NSD	47.1	48.1	*10.3**	**31.5***
HD	20.5	25.8	*3.7**	**11.5***
MHD	2.8	5.6	*0.3**	**1.6***
ACE	75.2	87.9	*14.8**	**47.3***
RI probability	32.7%	34.2%	*7.1%**	**37.5%***

FIG. 3. (a) Difference in VWS anomalies (m s^{-1}) between the AWB_area (+) and the AWB_area (−) [(g) minus (d)] during MJO phases 6–7. The AWB_area (+) comprises 472 days, and the AWB_area (−) consists of 524 days. Black dashed lines highlight the regions where differences in VWS between the two groups are significant at a 95% confidence level, and the purple line is the 2.4-PVU (1 PVU = 10^{-6} K kg^{-1} m^2 s^{-1}) contour at the 350-K isentropic surface in the AWB_area (+). (b) As in (a), but for differences in SST (shaded; K) and 10-m winds (vectors; m s^{-1}; only differences exceeding the 95% confidence level are shown). (c) As in (a), but for differences in TPW (shaded; kg m^{-2}) and column integrated moisture flux (vectors; kg m^{-1} s^{-1}; only differences exceeding the 95% confidence level are shown). (d)–(f) As in (a)–(c), but for anomalies in the AWB_area (−) during MJO phases 6–7. Anomalies are calculated from the long-term daily mean. (g)–(i) As in (d)–(f), but for anomalies in the AWB_area (+).

also decline noticeably, but the difference between the two groups fails to reach the 90% confidence level.

In contrast, occurrences of AWB are associated with a significant decrease for all TC metrics during phases 6–7 (Table 2). More than twice as many named storms and hurricanes occur in the AWB_area (−) compared with the AWB_area (+). Most other TC metrics decrease by over 60% from the AWB_area (+) to the AWB_area (−). The chance of a system undergoing at least one RI episode during its lifetime also varies considerably. TCs in the AWB_area (−) are 5 times more likely to experience RI than their counterparts in the AWB_area (+). Differences in basinwide TC activity between the two groups are further illustrated in Fig. S4. When AWB occurs, fewer TC tracks occur over the Gulf of Mexico and the northwestern

Atlantic (Fig. S4a). These results suggest that the impacts of AWB–MJO interaction on Atlantic TCs are nonlinear and may explain why subseasonal variability of AWB is weakly correlated with Atlantic TC activity in some years (Li et al. 2018). Occurrences of AWB play a key role in suppressing basinwide TC activity during phases 6–7, but not phases 2–3.

Our investigation now focuses on how large-scale environmental conditions are altered by AWB, particularly during phases 6–7. As evidenced by Figs. 3a–c, tropospheric moisture, VWS, and SSTs are significantly perturbed in the vicinity of breaking waves. The southwest–northeast tilt of the trough (Fig. 3a) transports eddy westerly momentum flux northward ($u'v' > 0$; Starr 1948), pushing the midlatitude eddy-driven jet poleward (Strong and Magnusdottir 2008) and leading to an
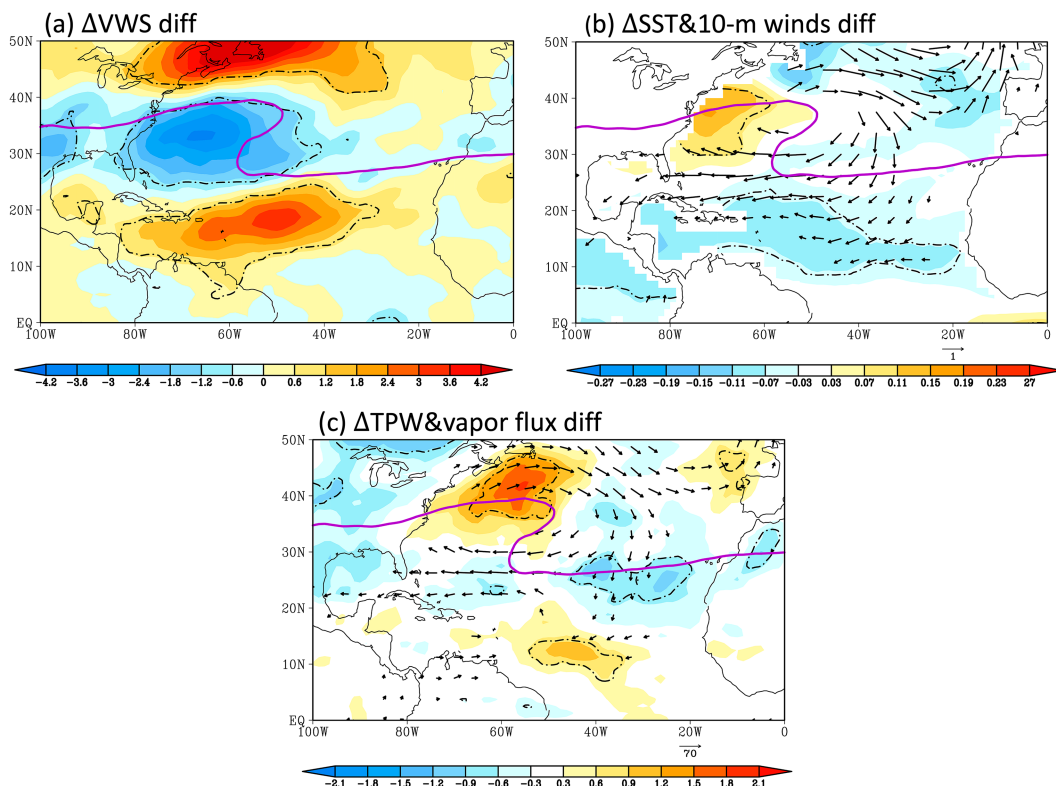
FIG. 4. As in Figs. 3a–c but for phases 2–3. The AWB_area (+) comprises 509 days, and the AWB_area (−) comprises 787 days.

increase of shear north of 40°N (Fig. 3a). Meanwhile, on the southern side of the high-PV tongue, the westerly wind tendency driven by the equatorward flux of extratropical cool air (Swenson and Straus 2017), along with the intensifying easterly trades in the lower troposphere (Fig. 3b), contributes to the lobe of positive VWS anomalies (Fig. 3a). Juxtaposed with the upper-level trough, an anomalous anticyclonic circulation develops at the surface and advects cool and dry air on its southeastern/southern sides, inducing cooling of SSTs over the tropical North Atlantic (Fig. 3b) through modulations of surface air–sea fluxes (Strong and Magnusdottir 2009; Zhang and Wang 2019), and potentially by ocean mixing. The surface anticyclonic anomalous flow also dominates the spatial pattern of horizontal moisture flux (see vectors in Fig. 3c). The strengthened southwesterly winds upstream of the AWB result in transport of moist and warm air from the tropical oceans to the east coast of North America (Fig. 3c). Within the high-PV tongue, anomalous northeasterly winds carry the dry air originating from the lower stratosphere downward and equatorward, leading to reduced TPW over a southwest–northeast band extending from the extratropical North Atlantic to the Caribbean Sea (Fig. 3c).

During MJO phases 6–7, even without the effect of AWB (Fig. S3d), significantly higher shear and lower SST are found over the central-to-western MDR (Figs. 3d,e). Dry anomalies occur over the central and eastern tropical–subtropical North Atlantic, Gulf of Mexico, and regions near the U.S. Atlantic

coast (Fig. 3f), all of which reduce the likelihood of TC development. Occurrences of AWB further intensify the amplitude of shear and SST anomalies south of 25°N (Figs. 3g,h). The anomalous shear magnitude exceeds 4 m s^{-1} over the Caribbean Sea (Fig. 3g). Regions characterized by enhanced shear and colder SSTs north of 10°N (Figs. 3g,h) are collocated with a pronounced reduction of TPW (Fig. 3i). Overall, AWB works together with MJO phases 6–7 to constructively suppress basinwide TC activity (Table 2) by creating an environment that is extremely unfavorable for TC genesis and development.

We next investigate why AWB leads to a significant suppression of basinwide TC activity in phases 6–7 but not in phases 2–3. To address this problem, we further examine the composite differences in VWS, SST, and TPW anomalies between the AWB_area (+) and AWB_area (−) during phases 2–3 (Fig. 4). Spatial distributions of the AWB-induced changes in shear, SST, and moisture during phases 2–3 (Fig. 4) are qualitatively consistent with those observed in phases 6–7 (Figs. 3a–c), but discrepancies between them are easily discernible.

Relative to wave breaking events in phases 2–3, AWB episodes in phases 6–7 are accompanied by slightly weaker VWS anomalies (Figs. 3a and 4a), but stronger negative anomalies of SST and TPW (Figs. 3b,c and 4b,c). Additionally, the centroid of the upper-level trough observed in phases 6–7 is displaced approximately 10° west of their phase 2–3 counterparts (see purple contours in Figs. 3a–c and 4). In both phases 2–3
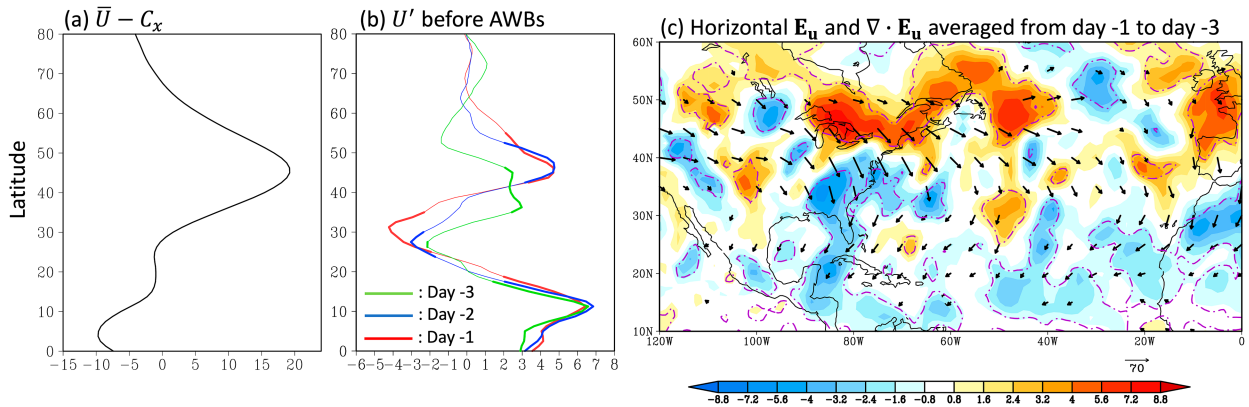
FIG. 5. (a) Composite difference (m s^{-1}) between the 200-hPa basic-state zonal wind ($\overline{U}$) and the wave's phase speed (C_x) as a function of latitude for 107 major AWB events. The difference is averaged between 90°– and 60°W. (b) Composited 200-hPa eddy zonal wind (m s^{-1}) at 70°W from day −3 to day −1. Differences significant at the 90% confidence level are highlighted by thick green, blue, and red lines. (c) Composited three-dimensional $\mathbf{E}_u$-flux divergence (shaded; m s^{-1} day^{-1}) and the horizontal components of the $\mathbf{E}_u$-flux vectors (m^2 s^{-2}) at 200 hPa. Dashed purple contours highlight the regions where the composited $\mathbf{E}_u$-flux divergence is significantly different from zero at the 90% confidence level.

and phases 6–7, an anomalous anticyclone develops at the surface (Figs. 3b and 4b), but the attendant northeasterly flow anomalies are stronger in phases 6–7. This drives enhanced SST cooling over the Atlantic MDR (Fig. 3b) by extracting more thermal energy from the ocean (not shown). The strengthened northeasterly winds also lead to enhanced equatorward transport of dry, stable air, resulting in stronger negative TPW anomalies over the Bahamas and the Caribbean Sea (Fig. 3c). Differences between Figs. 3a–c and Figs. 4a–c suggest that individual AWB events occurring in phases 6–7 may disturb the development of surrounding TCs and their precursors to a greater extent than their phases 2–3 counterparts, agreeing with previous findings (Galarneau et al. 2015; Zavadoff and Kirtman 2019; Zhang et al. 2017). Studies by Galarneau et al. (2015) and Zavadoff and Kirtman (2019) indicated that AWB events over the western part of North Atlantic are associated with more prevalent subsidence and tropospheric dryness, as well as a stronger anticyclone at the surface, when compared with breaking waves over the eastern Atlantic.

4. The physical mechanisms connecting the MJO and AWB

The importance of AWB events in suppressing Atlantic TCs during MJO phases 6–7 has spurred our interest to better understand the physical connections between the MJO and AWB. The established knowledge (Lee and Seo 2019; Sardeshmukh and Hoskins 1988; Seo and Son 2012; Seo and Lee 2017; Tseng et al. 2019; Wang et al. 2018) suggested that the propagating heating of MJO and its attendant anomalous divergence in the upper troposphere act as a Rossby wave source for poleward dispersing extratropical wave activity, inspiring our hypothesis that Rossby waves excited by enhanced intraseasonal convection over the Pacific propagate into the subtropical North Atlantic. These waves ultimately deform rapidly and irreversibly when the zonal background mean

flow cannot sustain their propagation. To validate this hypothesis, we first explore the flow evolution prior to the AWB events. Next, we seek to better understand the origin of Rossby waves that participate in the reversal of meridional PV gradients.

a. Flow evolution preceding AWB events and the role of transient eddy forcing

Since one AWB event typically lasts 1–3 days (Postel and Hitchman 2001; Zavadoff and Kirtman 2019; Zhang and Wang 2018) and is recorded at multiple 6-hourly time steps by the AWB detection algorithm, constructing the lead composites based on all of these time steps may count the same baroclinic wave several times. To avoid such repetition, we choose the day when the area of the equatorward high-PV tongue reaches its maxima as the reference time (i.e., day 0) to build the lead composites. Day 0 denotes the central date of a major AWB episode, and "day t" refers to t days relative to day 0. The following criteria are used to search for day 0: 1) the daily AWB_area anomaly averaged over the northwestern Atlantic (20°–35°N, 85°–45°W) is greater than one standard deviation, 2) the domain-averaged anomalous AWB_area value must be the largest within a time window of ±2 days, 3) the MJO phase at day 0 must be either 6 or 7, 4) the MJO amplitude at day 0 is greater than one, and 5) the MJO phase at day −2 and day −1 is 5, 6, or 7. A total of 107 major AWB events are tallied during phases 6–7 from 1974 to 2021.

Composite differences between the basic-state flow ($\overline{U}$) and the wave's phase speed (C_x) as a function of latitude for the 107 major AWB events are shown in Fig. 5a. Here $\overline{U}$ is defined as the 200-hPa zonal wind averaged from day −30 to day 0, and the averaged zonal phase speed C_x is estimated from the slope of the Hovmöller diagram (Fig. S5). As suggested by the anomalous 200-hPa meridional wind (Fig. S5a), geopotential height (Fig. S5b), and 350-K PV (Fig. S5c), a wave train approaches the U.S. East Coast from the North
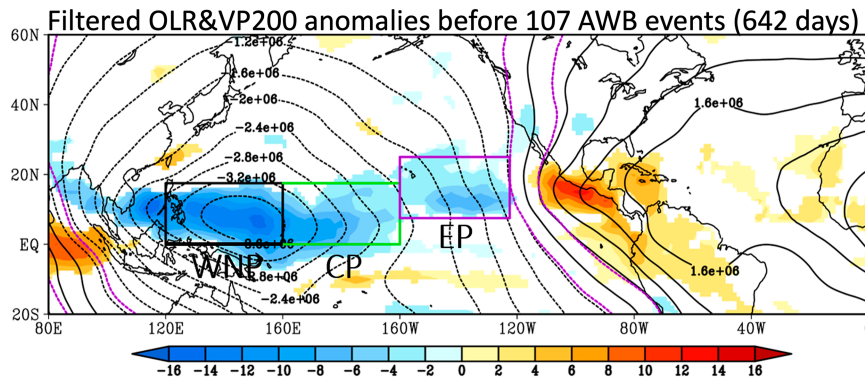
FIG. 6. Composited anomalies of 25–90-day bandpass-filtered OLR (shaded; W m^{-2}; only differences exceeding the 95% confidence level are shown) and 200-hPa velocity potential (contours; m^2 s^{-1}) averaged from day −9 to day −4 for 107 major AWB events. Purple dashed contours highlight 200-hPa velocity potential anomalies above the 95% confidence level.

Pacific sector prior to the occurrence of the 107 AWB events, with a zonal phase speed equal to ~6.5 m s^{-1}. As demonstrated by Fig. 5a, the midlatitude jet axis is located at 45°N, and the latitude where $\overline{U}$ is much larger than C_x (i.e., $\overline{U} - C_x > 5\,\mathrm{m\,s^{-1}}$) extends roughly from 35° to 55°N, suggesting that the westerly mean flow's support for Rossby wave propagation extends across at least 20° of latitude. On the other hand, the critical latitude, where the phase and mean flow speeds match, denotes the region of wave breaking (Held and Phillips 1990; Randel and Held 1991) and exists at ~30°N (Fig. 5a).

To better understand how the background mean flow evolves prior to the reversal of the PV gradient, the composite of eddy zonal winds (U') as a function of latitude is shown in Fig. 5b. For each AWB case, U' is defined as the departure from $\overline{U}$ at day t. From day −2 to day −1, significant deceleration occurs between 25° and 35°N (Fig. 5b), indicating a slight northward displacement of the critical latitude. In addition, mean flow changes could also affect the propagating direction of waves. As defined by Thorncroft et al. (1993), a refractive index for Rossby waves is inversely proportional to the value of $\overline{U} - C_x$. They suggested that the waves propagate toward the regions characterized by a higher refractive index. A smaller difference of $\overline{U} - C_x$ thus guides the waves to the equatorward side of the jet, and irreversible rearrangement of PV later occurs when the waves approach the critical layer.

A local Eliassen–Palm (EP) flux (Trenberth 1986) is utilized to better understand the Rossby wave propagation characteristics and diagnose the impact of transient eddies on the zonal mean flow. The direction of eddy heat and momentum transports can be inferred from the vectors of local EP flux, and the divergence (convergence) of local EP flux suggests that the transient eddy momentum and heat fluxes accelerate (decelerate) the background horizontal winds (Trenberth 1986). Here we focus on how the zonal motion is changed by the eddy forcing, and calculate the vector $\mathbf{E}_u$ and its divergence $\nabla \cdot \mathbf{E}_u$. Calculations for $\mathbf{E}_u$ and $\nabla \cdot \mathbf{E}_u$ are described in appendix B. Since significant deceleration begins from day −3 (Fig. 5b), we therefore average the horizontal component of $\mathbf{E}_u$ and the

three-dimensional divergence of the $\mathbf{E}_u$ flux at 200 hPa from day −3 to day −1 (Fig. 5c). The horizontal vector of $\mathbf{E}_u$ suggests that the upper-tropospheric eddies migrate eastward and equatorward across the United States. Additionally, patches of $\mathbf{E}_u$-flux convergence are visible over the southeastern United States and the northwestern subtropical Atlantic, which delineate an easterly torque on the mean zonal flow, with a magnitude exceeding 2 m s^{-1} day^{-1}. Therefore, eddy activity acts to decelerate the westerly flow near the critical latitude and also contributes to the acceleration of the jet between 40° and 50°N prior to the AWB events (Figs. 5b,c). The meridional dipole pattern of $\mathbf{E}_u$-flux divergence is representative of the rapid development of an upper-level ridge near the U.S. East Coast (Fig. S6). This has been regarded as a response to the enhanced latent heat release within the warm conveyor belt of extratropical cyclones (Knippertz and Martin 2007; Madonna et al. 2014; Zhang and Wang 2018).

b. Origin of the Rossby waves

According to past studies (Zavadoff and Kirtman 2019; Zhang and Wang 2018), roughly 1 week prior to AWB events, an embryonic upstream wave train pattern forms over the North Pacific. This wave train then amplifies ~72–96 h before the onset of the AWB event. Also, it typically takes at least five days for a specific phase of the MJO to force a distinct circulation response in the extratropics (Henderson et al. 2017; Tseng et al. 2019). Thus, MJO convective activity during the 4–9-day period before the AWB may play a critical role in amplifying the wave train. Figure 6 displays the 25–90-day band-passed filtered OLR and 200-hPa velocity potential (VP200) anomalies averaged from day −9 to day −4. Organized large-scale negative OLR anomalies extend from the Bay of Bengal to the eastern North Pacific. The largest OLR differences of ~14–16 W m^{-2} are observed over the tropical western Pacific warm pool (Fig. 6), since SST over this region is high enough to maintain convective instability (Zhang 2005). In the tropics, areas of enhanced upper-level divergence (i.e., negative VP200 anomalies) agree well with the regions where deep convection develops. In contrast to negative OLR anomalies over the tropical Pacific, convection in the
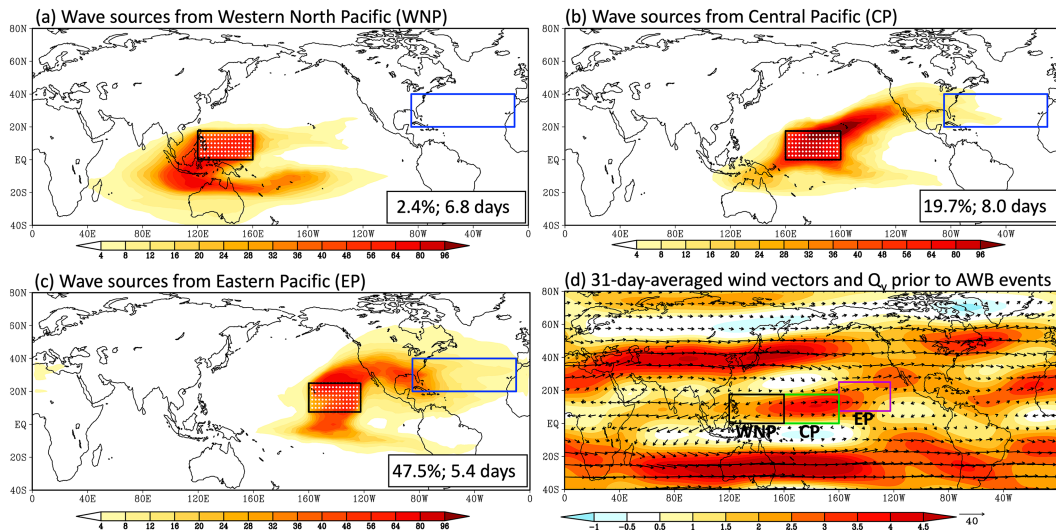
FIG. 7. (a) Mean track density of wave rays (unit: count per 10 days on a 2.5° × 2.5° grid for each initial k) emanated from the western North Pacific heat source (white dots within the black domain). The numbers located in the bottom right corner represent the ratio (%) of rays that reach the subtropical North Atlantic (20°–40°N, 85°–10°W, denoted by the blue domain) as well as the average travel time (days) required for the waves to arrive in the subtropical North Atlantic. (b),(c) As in (a), but for wave rays initiated from the central Pacific and the eastern North Pacific, respectively. (d) Composited horizontally nonuniform basic flow (vectors; m s^{-1}) and the meridional gradient of absolute vorticity Q_y (shaded; 10^{-11} m^{-1} s^{-1}) for 107 major AWB events.

eastern Pacific adjacent to the Central American coast, Caribbean Sea, and the eastern MDR is significantly suppressed (Fig. 6).

The large-scale convective centers of the MJO in the tropical Indian and Pacific Oceans excite poleward-propagating Rossby waves that can cause significant anomalies in the extratropical circulation (Matthews et al. 2004; Seo and Son 2012; Seo and Lee 2017). Therefore, regions with negative OLR anomalies (Fig. 6), including the western North Pacific (WNP; 0°–17.5°N, 120°–160°E), the central Pacific (CP; 0°–17.5°N, 160°E–160°W), and the eastern North Pacific (EP; 7.5°–22.5°N, 160°–122.5°W), are used to seed the Rossby waves at 200 hPa (see the white dots in Figs. 7a–c). To better characterize the overall behavior of wave energy propagation, we calculate large samples of wave rays with different starting locations, initial wavenumbers, and background flow states, as ray trajectories are known to be affected by changes in these quantities (Garfinkel et al. 2022; Li et al. 2015, 2019; Li et al. 2020; Sakaguchi et al. 2016). For the initial zonal wavenumber (k), we consider ranges from 1 to 8 since short waves with an initial k larger than 8 are likely trapped after a short-term integration (~8 h; Li et al. 2019). Also, the waves are assumed to be nonstationary given the positive phase speed (i.e., $C_x = 6.5$ m s^{-1}; Fig. S5). As mentioned previously, the horizontally nonuniform basic flow is the 200-hPa winds averaged from day −30 to day 0. This flow varies between different AWB events. Therefore, for rays originating from a specific domain, we replace the basic states with 107 different realizations and obtain a large size of wave rays (>100 000 members). By diagnosing this large sample, we can quantify the propagation properties of Rossby waves.

Figures 7a–c show the mean track density of wave trajectories emanating from the WNP, CP, and EP sources, respectively. The wave rays from the WNP source region show significant southwestward cross-equatorial propagation (Fig. 7a). Once the waves reach the south Indian Ocean, they turn to propagate eastward along the northern flank of the subtropical jet (Figs. 7a,d). Our results support the findings by Li et al. (2015) and Zhao et al. (2019) that the summertime northeasterly winds above the Australian-Asian monsoon region play a key role in interhemispheric transmission of wave energy in the upper troposphere. Nevertheless, the southward-propagating waves excited by the western Pacific heat source fail to explain why AWB preferentially occurs over the western North Atlantic during MJO phases 6–7.

When the rays are initialized from the CP source, they display a preferred pathway from the basepoint northeastward to the west coast of North America. A total of 19.7% of waves arrive in the subtropical North Atlantic [20°–40°N, 85°–10°W; the same domain as defined in Zhang et al. (2017)] within 10 days, and the density distribution of the wave trajectory is more concentrated in the central Pacific north of 15°N (Fig. 7b). The relatively weak westerly waveguide over this region appears to be responsible for the slow propagation of waves (Fig. 7d). Rossby wave packets that arise from the EP region tend to propagate northeastward across the southern United States, later reaching the Gulf of Mexico and the western part of North Atlantic (Fig. 7c). Figure 7c displays the highest wave track density over the subtropical North Atlantic. Furthermore, nearly half of the waves that originate from the EP region reach the North Atlantic sector within 5–6 days. These results suggest
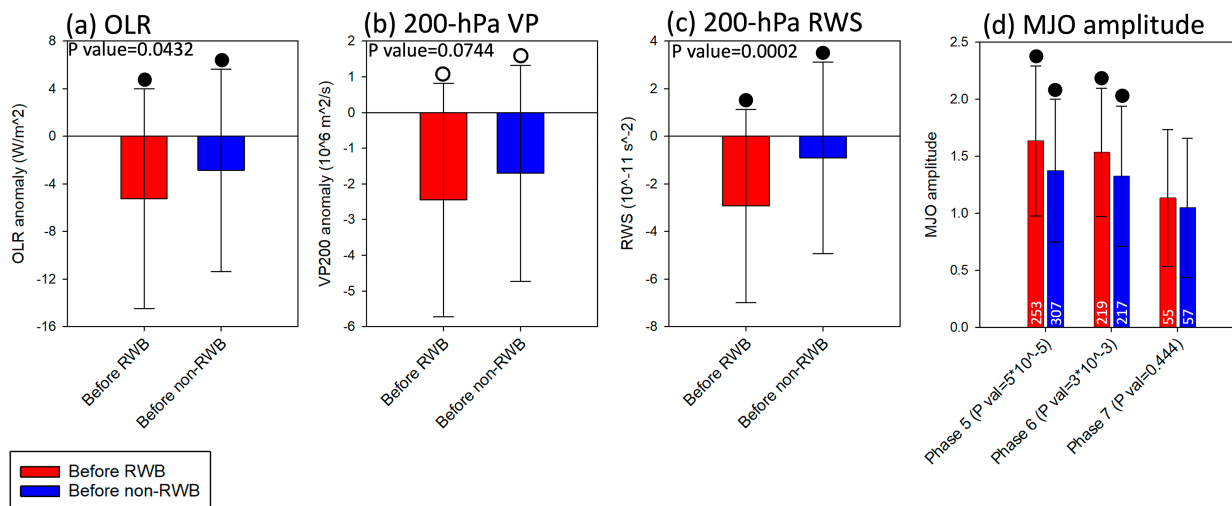
FIG. 8. (a) OLR anomalies (W m^{-2}) averaged over the eastern North Pacific in the 4–9-day period prior to AWB day 0 (red bar) and non-AWB day 0 (blue bar). Whiskers are standard deviations between different events, and black solid dots indicate that the difference between the two groups is significant at a 95% confidence level. (b) As in (a), but for VP200 anomalies (10^6 m^2 s^{-1}). Black hollow dots indicate that the difference between the two groups is significant at a 90% confidence level. (c) As in (a), but for 200-hPa RWS (10^{-11} s^{-2}). (d) Mean amplitudes of the RMM index during phases 5–7 in the 4–9-day period prior to AWB day 0 (red bars) and non-AWB day 0 (blue bars), along with their corresponding standard deviations (whiskers). The whiskers indicate the standard deviation in amplitudes across different days. The number of days in different RMM phases is denoted by the white values at the bottom.

that enhanced tropical convection over the EP plays a leading role in facilitating southeastward penetration of synoptic waves into the subtropical Atlantic, thereby increasing the likelihood of wave breaking over the Gulf of Mexico and Greater Antilles. On the other hand, fluctuations of convective heat sources over the CP could also contribute to variations of AWB events (Fig. 7b), but to a lesser extent. Although the current results are based on the background flows averaged from day −30 to day 0, additional analyses indicate that the overall propagation behavior of waves is not sensitive to the period used to calculate the basic states (Fig. S7).

The previous ray tracing results guide us to investigate whether the occurrences of AWB are preceded by enhanced convectively forced Rossby wave source in the eastern North Pacific. To facilitate an objective comparison with day 0 of the AWB events, we identify the day when the spatial extent of equatorward-intruding high-PV tongue is anomalously small. This day is referred to as "non-AWB day 0". See the online supplemental material for detailed definitions of non-AWB day 0. During phases 6–7, the sample size of non-AWB day 0 equals 127, and each of these days corresponds to a period characterized by suppressed AWB activity. OLR anomalies averaged over the EP in the 4–9-day period before AWB day 0 and non-AWB day 0 are shown in Fig. 8a, respectively; and domain-averaged VP200 anomalies for these two groups are compared in Fig. 8b. Both OLR and VP200 anomalies show significant differences between the two groups, indicating that stronger convectively forced upper-level divergence leads up to major AWB episodes (Figs. 8a,b).

The Rossby wave source (RWS) is often used to diagnose the origin of the propagating Rossby wave (Lau and Peno

1992; Seo and Lee 2017; Sardeshmukh and Hoskins 1988). It can be expressed as

$$\text{RWS} = -\nabla \cdot (v_x \zeta_a) , \qquad (4)$$

where v_x represents the divergent component of horizontal winds and ζ_a denotes the absolute vorticity. In the Northern Hemisphere, the upper-level divergence acts on a region with positive absolute vorticity gradients and generates an anomalous negative RWS in the upper troposphere (Sardeshmukh and Hoskins 1988). Before AWB events, the significantly larger amplitude of RWS (Fig. 8c) suggests that Rossby waves can be generated more efficiently over the EP. Furthermore, there is a significant increase in the amplitude of phases 5–6 before AWB day 0, which is consistent with enhanced convective outflow (Figs. 8a,b). Overall, the above analyses suggest that the strength of convective activity over the eastern Pacific and the phase 5–6 amplitude may serve as predictors for the extended-range forecast of wave breaking events over the subtropical Atlantic during phases 6–7.

In addition to the influence of convectively driven Rossby wave source, we further explore the impact of upper-level zonal wind on the propagation of Rossby waves by examining the stationary zonal wavenumber K_s (Hoskins and Ambrizzi 1993; Karoly 1983). Detailed calculations of K_s can be found in the online supplemental material. It is known that Rossby waves tend to propagate toward regions with larger K_s, indicating the intensity of the waveguide (Hoskins and Ambrizzi 1993). Before AWB day 0, we observe relatively higher values of K_s over the Gulf of Mexico and the western part of the subtropical Atlantic, which can be further attributed to the reduced 200-hPa zonal winds over this region (Fig. S8). Consequently,

the enhanced Rossby wave source over the tropical EP, coupled with the expanded waveguide, can both contribute to the occurrences of AWB during phases 6–7.

5. Discussion and conclusions

Atlantic TC activity is influenced by different modes of variability across a range of time scales (Camargo et al. 2010). As the dominant mode of intraseasonal variability in the tropical atmosphere (Madden and Julian 1972; Zhang 2005), the MJO considerably impacts the likelihood of TC genesis and intensification in the Gulf of Mexico and the tropical North Atlantic (Aiyyer and Molinari 2008; Klotzbach 2010, 2012; Klotzbach and Oliver 2015b; Ventrice et al. 2011). Nevertheless, the MJO alone does not completely explain Atlantic subseasonal TC variability. Extratropical weather perturbations, particularly AWB, have also been recognized as an important contributor to the intraseasonal variability of Atlantic TCs (Li et al. 2018; Papin et al. 2023; Zhang et al. 2016). Therefore, this study seeks to better understand how the nonlinear interaction of the MJO and AWB work to influence Atlantic TC activity. Our findings indicate that the MJO and AWB work constructively to suppress basinwide TC activity during phases 6–7, but not during phases 2–3. Furthermore, we find that the MJO can regulate the probability of AWB over the western subtropical Atlantic mainly by changing the convectively forced Rossby wave source over the tropical eastern Pacific.

We find that the Gulf of Mexico and Atlantic MDR experience enhanced basinwide TC activity when the convectively active phase of the MJO occurs over the Indian Ocean. Various measures of TC activity, including storm counts, hurricanes, major hurricanes, named storm days, and ACE exhibit a significant increase. Conversely, when the MJO convection shifts from the Indian Ocean to the central-to-eastern Pacific, a decrease of TCs in the North Atlantic is observed. Our analysis aligns with previous studies (Aiyyer and Molinari 2008; Klotzbach 2010, 2012; Klotzbach and Oliver 2015b; Maloney and Shaman 2008) and suggests that the MJO influences Atlantic TCs primarily through modulation of various environmental conditions and synoptic wave activity. Furthermore, the likelihood of AWB over the western part of the subtropical Atlantic is significantly enhanced during phases 6–7 but reduced during phases 2–3, partly explaining the contrasting TC activity observed during different MJO phases.

Although the probability of AWB occurrence in the northwestern Atlantic varies significantly across different MJO phases, variations of AWB events can also be driven by other factors. For instance, the propagation of midlatitude Rossby waves and their ensuing breaking over the North Atlantic can be affected by the synoptic weather regimes over the PNA sector (Zhang and Wang 2019). Such extratropical flow variability may not be strongly influenced by the MJO during the warm season (Zhou et al. 2012). Considering that AWB can occur during the entire life cycle of the MJO, it is crucial to understand how adverse effects of the AWB on Atlantic TCs differ between various MJO phases. Our analyses demonstrate that AWB events considerably restrain the development and genesis

of TCs in phases 6–7, while their adverse impact is less pronounced in phases 2–3.

During phases 6–7, when high-PV air penetrates downward and equatorward, the numbers of named storms, hurricanes, major hurricanes, named storm days, hurricane days, major hurricane days, and ACE decrease by ∼50%–80%. Furthermore, the probability of a TC undergoing at least one RI episode during its lifetime decreases to near zero. Simultaneously, large-scale environmental conditions, such as VWS, precipitable water, and SSTs, become anomalously unfavorable for TC genesis and strengthening, when compared to periods without a reversed meridional PV gradient. Further investigation reveals that AWB events during phases 6–7 tend to be located closer to the U.S. East Coast compared to those occurring in phases 2–3. Additionally, AWB events during phases 6–7 are associated with the development of a stronger anticyclone in the lower troposphere, which transports more dry, stable extratropical air into the tropical environment and drives enhanced tropical SST cooling. Consequently, individual AWB events during phases 6–7 can more effectively suppress convection within the high-PV tongue, potentially disrupting the development of adjacent TCs to a greater extent than their phase 2–3 counterparts.

The convective heating of the MJO can excite Rossby waves, which disperse poleward and establish a teleconnection pattern across the Pacific–North American sector in winter (e.g., Mori and Watanabe 2008; Seo and Son 2012; Seo and Lee 2017; Tseng et al. 2019). We therefore assume that similar physical mechanisms may also operate during the Atlantic hurricane season, though seasonal changes in the background mean state could affect Rossby wave propagation. Active MJO convection dominates the entire tropical Pacific before AWB occurrences during phases 6–7. Wave rays originating from the tropical western Pacific travel southwestward toward the Southern Hemisphere. Conversely, the intensified tropical convection over the eastern Pacific acts as an extra source of Rossby waves and, in conjunction with the expanded waveguide, plays a central role in facilitating the southeastward penetration of extratropical waves into the Gulf of Mexico and the Greater Antilles. This, in turn, increases the likelihood of wave breaking in this region. Fluctuations in convective heat sources over the central Pacific can also influence the activity of Rossby waves over the North Atlantic, albeit to a lesser extent. As the Rossby wave packets move into the northwestern subtropical Atlantic, the transient eddy forcing associated with the rapid development of an upper-level ridge near the U.S. East Coast decelerates the westerly mean flow between 25° and 35°N. Variations in the background zonal flow cause a northward shift of the critical latitude and increase the refractive index south of the jet, facilitating equatorward propagation of waves, ultimately resulting in wave breaking as they approach the critical layer.

Since the enhanced convection and upper-level divergence over the eastern Pacific serve as an effective Rossby wave source for subsequent wave-breaking events over the North Atlantic, it is natural to explore the factors that sustain or intensify the convective signal of the MJO over the central-to-eastern Pacific. As suggested by Wang and Li (2021), an El Niño–like background SST anomaly can boost intraseasonal precipitation over the central Pacific and promote MJO convection moving farther into

the eastern Pacific. Another factor that affects convective strength over the eastern Pacific is whether the MJO can cross the Maritime Continent (MC). Fu et al. (2018) reported that boreal-summer MJOs exhibit three downstream fates after reaching the MC, namely smooth transition (type I), rapid decay (type II), or significant intensification (type III). Type I and type III events are associated with relatively strong convection over the central-to-eastern Pacific. For these MJO events, the continuous eastward propagation of deep convection is associated with premoistening over the western Pacific, which is mainly attributed to enhanced boundary layer convergence driven by equatorial Kelvin waves (Fu et al. 2018; Hendon and Salby 1994; Hsu and Lee 2005; Jones and Weare 1996; Wang and Li 1994). Type I and type III events may be indicative of frequent AWB occurrences during phases 6–7 over the North Atlantic, but this hypothesis requires further testing.

It is important to note that propagating Rossby waves can originate from various meteorological processes other than the upper-level divergent flow associated with the MJO. For instance, the diabatic heating associated with extratropical cyclones (Chang et al. 2002), interactions between recurving TCs and extratropical flow over the North Pacific (Archambault et al. 2015), and the convective outflow of the Asian monsoon (Postel and Hitchman 2001) can create or amplify Rossby wave packets. Therefore, the intraseasonal convection over the eastern Pacific is just one of several pathways that trigger Rossby waves propagating toward the North Atlantic. Moreover, future studies could explore how AWB and Atlantic TCs respond to intensified intraseasonal precipitation over the eastern Pacific. The MJO is projected to propagate further into the central and eastern tropical Pacific, and its average amplitude is expected to increase as the climate warms (Bui and Maloney 2018; Chang et al. 2015; Subramanian et al. 2014).

We caution that the extratropical circulation patterns associated with the MJO exhibit significant differences between summer and winter due to the strong seasonal cycle of both the MJO itself and basic states (Ambrizzi et al. 1995; Ambrizzi and Hoskins 1997; Hagos et al. 2019, 2020; Zhang and Dong 2004). First, the location of enhanced intraseasonal convection and circulation is known to shift with the seasons (Adames et al. 2016; Knutson and Weickmann 1987; Salby and Hendon 1994; Zhang and Dong 2004). In the tropical northeastern Pacific, the MJO convective signals are much stronger during boreal summer than winter (Knutson and Weickmann 1987; Maloney and Kiehl 2002; Zhang and Dong 2004), possibly due to the expansion of the Western Hemisphere warm pool in the boreal spring (Wang and Enfield 2001, 2003). In contrast, compared to winter, the precipitation and wind signals associated with the MJO slightly weaken and shift north of the equator in the western Pacific (Zhang and Dong 2004). Second, MJO teleconnections are highly dependent on the spatial structure of the tropospheric

westerly jet (Henderson et al. 2017; Wang et al. 2020). During boreal summer, the waveguide displaces poleward and weakens due to seasonal changes in the tropospheric westerly jet (Ambrizzi et al. 1995; Ambrizzi and Hoskins 1997). Consequently, the extratropical circulation becomes less sensitive to forcing by a near-equatorial heat source, resulting in a weaker Rossby wave response in the summer hemisphere (Adames et al. 2016).

Despite the weaker wave response, our study proposes a plausible mechanism by which tropical forcing over the eastern Pacific can affect North Atlantic TCs through changing the behavior of Rossby waves. The pathway involves enhanced MJO convective anomalies over the northeastern Pacific, serving as an additional Rossby wave source. Changes in the waveguide further allow more waves to propagate and break over the North Atlantic, ultimately modulating subseasonal Atlantic TC activity. Thus, our study suggests a summertime teleconnection between the tropical eastern Pacific and the North Atlantic.

Data availability statement. JRA-55 data are available through the NCAR Research Data Archive (RDA) (https:// rda.ucar.edu/datasets/ds628.0/). HURDAT2 was provided by the Atlantic Oceanographic and Meteorological Laboratory (AOML)/NOAA Hurricane Research Division (https://www. nhc.noaa.gov/data/#hurdat). NOAA OLR data are available from https://psl.noaa.gov/data/gridded/data.olrcdr.interp.html, and the RMM index is available from http://www.bom.gov.au/ climate/mjo/graphics/rmm.74toRealtime.txt.

APPENDIX A

Calculating AWB Areal Fraction

Here we define domain A, which is determined by the zonal and meridional boundaries of the high-PV tongue, as the region affected by the AWB. See the schematic shown in Fig. A1 for further clarity.
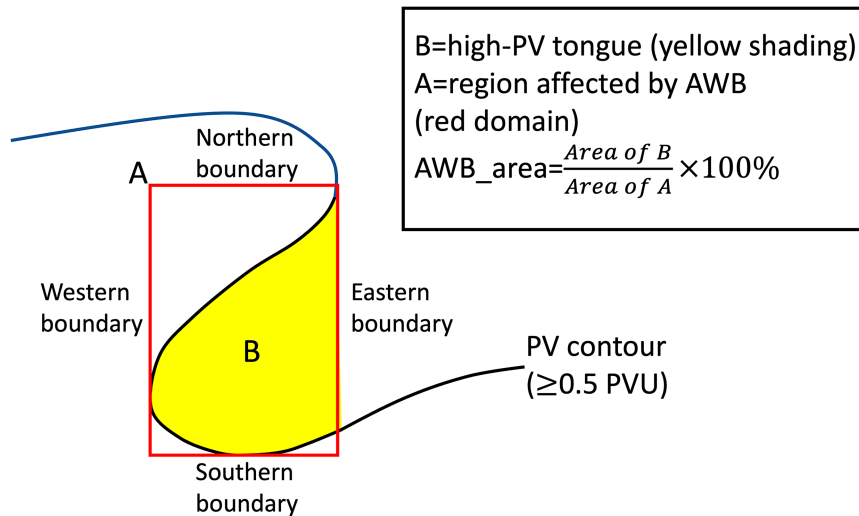
FIG. A1. Schematic diagram showing how to estimate the fraction of a certain domain covered by high-PV air. The region affected by the AWB is defined by the zonal and meridional boundaries of the high-PV tongue, and the yellow shading indicates the spatial extent of the equatorward-intruding trough.

APPENDIX B

Local EP Flux (Vector) $\mathbf{E}_u$ and Its Divergence ($\nabla \cdot \mathbf{E}_u$)

According to Trenberth (1986), the three-dimensional local EP flux vector ($\mathbf{E}_u$) can be expressed by

$$\mathbf{E}_u = \left[\frac{1}{2}(\overline{v'^2} - \overline{u'^2}), \; -\overline{u'v'}, \; fR\frac{\overline{v'T'}}{S}\right]\cos\phi, \quad (B1)$$

where the three-dimensional gradient operators are expressed as

$$\nabla = \left[\frac{\partial}{\partial x}, \; \frac{1}{\cos\phi}\frac{\partial}{\partial y}\cos\phi, \; \frac{1}{\rho_0}\frac{\partial}{\partial z}\rho_0\right]. \quad (B2)$$

Here,

$$z = \ln\left(\frac{P_0}{P}\right), \quad (B3)$$

$$S = R\left[\frac{\partial T}{\partial z} + 0.286T\right], \quad \text{and} \quad (B4)$$

$$\rho_0(z) = \rho_s e^{-z}. \quad (B5)$$

The overbars denote time averaging, and the primes are the eddy components, defined as the departures from the 31-day time mean averaged from day -30 to day 0. Equations (B1)–(B5) involve zonal and meridional winds (u, v), temperature (T), the Coriolis parameter (f), the ideal gas constant (R), latitude (ϕ), pressure (P), surface air density (ρ_s), static stability (S), and $P_0 = 1000$ hPa. Here the local EP flux divergence ($\nabla \cdot \mathbf{E}_u$) can be decomposed into the horizontal and vertical components, $\nabla \cdot \mathbf{E}_H$ and $\nabla \cdot \mathbf{E}_V$, respectively:

$$\nabla \cdot \mathbf{E}_u = \nabla \cdot \mathbf{E}_H + \nabla \cdot \mathbf{E}_V. \quad (B6)$$

Note that $\nabla \cdot \mathbf{E}_H$ represents the impact from horizontal transient eddy momentum fluxes, and the vertical component $\nabla \cdot \mathbf{E}_V$ denotes the influence from transient eddy heat fluxes.

REFERENCES

Abatzoglou, J. T., and G. Magnusdottir, 2006: Planetary wave breaking and nonlinear reflection: Seasonal cycle and interannual variability. *J. Climate*, **19**, 6139–6152, https://doi.org/10.1175/JCLI3968.1.

Adames, Á. F., J. M. Wallace, and J. M. Monteiro, 2016: Seasonality of the structure and propagation characteristics of the MJO. *J. Atmos. Sci.*, **73**, 3511–3526, https://doi.org/10.1175/JAS-D-15-0232.1.

Aiyyer, A., and J. Molinari, 2008: MJO and tropical cyclogenesis in the Gulf of Mexico and eastern Pacific: Case study and idealized numerical modeling. *J. Atmos. Sci.*, **65**, 2691–2704, https://doi.org/10.1175/2007JAS2348.1.

Alaka, G. J., Jr., and E. D. Maloney, 2012: The influence of the MJO on upstream precursors to African easterly waves. *J. Climate*, **25**, 3219–3236, https://doi.org/10.1175/JCLI-D-11-00232.1.

Ambrizzi, T., and B. J. Hoskins, 1997: Stationary Rossby-wave propagation in a baroclinic atmosphere. *Quart. J. Roy. Meteor. Soc.*, **123**, 919–928, https://doi.org/10.1002/qj.49712354007.

——, ——, and H.-H. Hsu, 1995: Rossby wave propagation and teleconnection patterns in the austral winter. *J. Atmos. Sci.*, **52**, 3661–3672, https://doi.org/10.1175/1520-0469(1995)052<3661:RWPATP>2.0.CO;2.

Archambault, H. M., D. Keyser, L. F. Bosart, C. A. Davis, and J. M. Cordeira, 2015: A composite perspective of the extratropical flow response to recurring western North Pacific

tropical cyclones. *Mon. Wea. Rev.*, **143**, 1122–1141, https://doi.org/10.1175/MWR-D-14-00270.1.

Balaguru, K., L. R. Leung, S. M. Hagos, and S. Krishnakumar, 2021: An oceanic pathway for Madden–Julian Oscillation influence on Maritime Continent tropical cyclones. *npj Climate Atmos. Sci.*, **4**, 52, https://doi.org/10.1038/s41612-021-00208-4.

Barrett, B. S., and L. M. Leslie, 2009: Links between tropical cyclone activity and Madden–Julian Oscillation phase in the North Atlantic and northeast Pacific basins. *Mon. Wea. Rev.*, **137**, 727–744, https://doi.org/10.1175/2008MWR2602.1.

Bell, G. D., and Coauthors, 2000: Climate assessment for 1999. *Bull. Amer. Meteor. Soc.*, **81** (6), S1–S50, https://doi.org/10.1175/1520-0477(2000)81[s1:CAF]2.0.CO;2.

Benedict, J. J., S. Lee, and S. B. Feldstein, 2004: Synoptic view of the North Atlantic Oscillation. *J. Atmos. Sci.*, **61**, 121–144, https://doi.org/10.1175/1520-0469(2004)061<0121:SVOTNA>2.0.CO;2.

Bentley, A. M., L. F. Bosart, and D. Keyser, 2017: Upper-tropospheric precursors to the formation of subtropical cyclones that undergo tropical transition in the North Atlantic basin. *Mon. Wea. Rev.*, **145**, 503–520, https://doi.org/10.1175/MWR-D-16-0263.1.

Brunet, G., and Coauthors, 2010: Collaboration of the weather and climate communities to advance subseasonal-to-seasonal prediction. *Bull. Amer. Meteor. Soc.*, **91**, 1397–1406, https://doi.org/10.1175/2010BAMS3013.1.

Bui, H. X., and E. D. Maloney, 2018: Changes in Madden-Julian Oscillation precipitation and wind variance under global warming. *Geophys. Res. Lett.*, **45**, 7148–7155, https://doi.org/10.1029/2018GL078504.

Camargo, S. J., M. C. Wheeler, and A. H. Sobel, 2009: Diagnosis of the MJO modulation of tropical cyclogenesis using an empirical index. *J. Atmos. Sci.*, **66**, 3061–3074, https://doi.org/10.1175/2009JAS3101.1.

——, A. H. Sobel, A. G. Barnston, and P. J. Klotzbach, 2010: The influence of natural climate variability on tropical cyclones, and seasonal forecasts of tropical cyclone activity. *Global Perspectives on Tropical Cyclones, from Science to Mitigation*, 2nd ed. J. C. L. Chan and J. D. Kepert, Eds., World Scientific, 325–362.

Camp, J., and Coauthors, 2018: Skilful multiweek tropical cyclone prediction in ACCESS-S1 and the role of the MJO. *Quart. J. Roy. Meteor. Soc.*, **144**, 1337–1351, https://doi.org/10.1002/qj.3260.

Cassou, C., 2008: Intraseasonal interaction between the Madden–Julian Oscillation and the North Atlantic Oscillation. *Nature*, **455**, 523–527, https://doi.org/10.1038/nature07286.

Chang, C.-C., and Z. Wang, 2018: Relative impacts of local and remote forcing on tropical cyclone frequency in numerical model simulations. *Geophys. Res. Lett.*, **45**, 7843–7850, https://doi.org/10.1029/2018GL078606.

Chang, C.-W. J., W.-L. Tseng, H.-H. Hsu, N. Keenlyside, and B.-J. Tsuang, 2015: The Madden-Julian Oscillation in a warmer world. *Geophys. Res. Lett.*, **42**, 6034–6042, https://doi.org/10.1002/2015GL065095.

Chang, E. K. M., S. Lee, and K. L. Swanson, 2002: Storm track dynamics. *J. Climate*, **15**, 2163–2183, https://doi.org/10.1175/1520-0442(2002)015<2163:STD>2.0.CO;2.

Charney, J. G., and M. E. Stern, 1962: On the stability of internal baroclinic jets in a rotating atmosphere. *J. Atmos. Sci.*, **19**, 159–172, https://doi.org/10.1175/1520-0469(1962)019<0159:OTSOIB>2.0.CO;2.

Chiang, J. C. H., and D. J. Vimont, 2004: Analogous Pacific and Atlantic meridional modes of tropical atmosphere–ocean variability. *J. Climate*, **17**, 4143–4158, https://doi.org/10.1175/JCLI4953.1.

Davis, C. A., and L. F. Bosart, 2004: The TT problem: Forecasting the tropical transition of cyclones. *Bull. Amer. Meteor. Soc.*, **85**, 1657–1662, https://doi.org/10.1175/BAMS-85-11-1657.

Fjortoft, R., 1950: Application of integral theorems in deriving criteria of stability for laminar flows and for the baroclinic circular vortex. *Geophys. Publ.*, **17**, 1–52.

Frank, W. M., and P. E. Roundy, 2006: The role of tropical waves in tropical cyclogenesis. *Mon. Wea. Rev.*, **134**, 2397–2417, https://doi.org/10.1175/MWR3204.1.

Fu, J.-X., W. Wang, H.-L. Ren, X. Jia, and T. Shinoda, 2018: Three different downstream fates of the boreal-summer MJOs on their passages over the Maritime Continent. *Climate Dyn.*, **51**, 1841–1862, https://doi.org/10.1007/s00382-017-3985-2.

Funatsu, B. M., and D. W. Waugh, 2008: Connections between potential vorticity intrusions and convection in the eastern tropical Pacific. *J. Atmos. Sci.*, **65**, 987–1002, https://doi.org/10.1175/2007JAS2248.1.

Galarneau, T. J., Jr., R. McTaggart-Cowan, L. F. Bosart, and C. A. Davis, 2015: Development of North Atlantic tropical disturbances near upper-level potential vorticity streamers. *J. Atmos. Sci.*, **72**, 572–597, https://doi.org/10.1175/JAS-D-14-0106.1.

Garfinkel, C. I., W. Chen, Y. Li, C. Schwartz, P. Yadav, and D. Domeisen, 2022: The winter North Pacific teleconnection in response to ENSO and the MJO in operational subseasonal forecasting models is too weak. *J. Climate*, **35**, 8013–8030, https://doi.org/10.1175/JCLI-D-22-0179.1.

Goldenberg, S. B., C. W. Landsea, A. M. Mestas-Nuñez, and W. M. Gray, 2001: The recent increase in Atlantic hurricane activity: Causes and implications. *Science*, **293**, 474–479, https://doi.org/10.1126/science.1060040.

Hagos, S., C. Zhang, L. R. Leung, C. D. Burleyson, and K. Balaguru, 2019: A zonal migration of monsoon moisture flux convergence and the strength of Madden-Julian Oscillation events. *Geophys. Res. Lett.*, **46**, 8554–8562, https://doi.org/10.1029/2019GL083468.

——, ——, O. Garuba, C. D. Burleyson, and K. Balaguru, 2020: Impacts of insolation and soil moisture on the seasonality of interactions between the Madden-Julian Oscillation and Maritime Continent. *J. Geophys. Res. Atmos.*, **125**, e2020JD032382, https://doi.org/10.1029/2020JD032382.

Hanley, D., J. Molinari, and D. Keyser, 2001: A composite study of the interactions between tropical cyclones and upper-tropospheric troughs. *Mon. Wea. Rev.*, **129**, 2570–2584, https://doi.org/10.1175/1520-0493(2001)129<2570:ACSOTI>2.0.CO;2.

Hansen, K. A., S. J. Majumdar, and B. P. Kirtman, 2020: Identifying subseasonal variability relevant to Atlantic tropical cyclone activity. *Wea. Forecasting*, **35**, 2001–2024, https://doi.org/10.1175/WAF-D-19-0260.1.

Held, I. M., and P. J. Phillips, 1990: A barotropic model of the interaction between the Hadley cell and a Rossby wave. *J. Atmos. Sci.*, **47**, 856–869, https://doi.org/10.1175/1520-0469(1990)047<0856:ABMOTI>2.0.CO;2.

Henderson, S. A., and E. D. Maloney, 2013: An intraseasonal prediction model of Atlantic and East Pacific tropical cyclone genesis. *Mon. Wea. Rev.*, **141**, 1925–1942, https://doi.org/10.1175/MWR-D-12-00268.1.

——, ——, and S.-W. Son, 2017: Madden–Julian oscillation Pacific teleconnections: The impact of the basic state and MJO representation in general circulation models. *J. Climate*, **30**, 4567–4587, https://doi.org/10.1175/JCLI-D-16-0789.1.

Hendon, H. H., and M. L. Salby, 1994: The life cycle of the Madden–Julian oscillation. *J. Atmos. Sci.*, **51**, 2225–2237, https://doi.org/10.1175/1520-0469(1994)051<2225:TLCOTM>2.0.CO;2.

——, and J. Glick, 1997: Intraseasonal air–sea interaction in the tropical Indian and Pacific Oceans. *J. Climate*, **10**, 647–661, https://doi.org/10.1175/1520-0442(1997)010<0647:IASIIT>2.0.CO;2.

Hopsch, S. B., C. D. Thorncroft, K. Hodges, and A. Aiyyer, 2007: West African storm tracks and their relationship to Atlantic tropical cyclones. *J. Climate*, **20**, 2468–2483, https://doi.org/10.1175/JCLI4139.1.

Hoskins, B. J., and T. Ambrizzi, 1993: Rossby wave propagation on a realistic longitudinally varying flow. *J. Atmos. Sci.*, **50**, 1661–1671, https://doi.org/10.1175/1520-0469(1993)050<1661:RWPOAR>2.0.CO;2.

Hsu, H.-H., and M.-Y. Lee, 2005: Topographic effects on the eastward propagation and initiation of the Madden–Julian oscillation. *J. Climate*, **18**, 795–809, https://doi.org/10.1175/JCLI-3292.1.

Jiang, X., B. Xiang, M. Zhao, T. Li, S.-J. Lin, Z. Wang, and J.-H. Chen, 2018: Intraseasonal tropical cyclogenesis prediction in a global coupled model system. *J. Climate*, **31**, 6209–6227, https://doi.org/10.1175/JCLI-D-17-0454.1.

Jones, C., and B. C. Weare, 1996: The role of low-level moisture convergence and ocean latent heat fluxes in the Madden and Julian oscillation: An observational analysis using ISCCP data and ECMWF analyses. *J. Climate*, **9**, 3086–3104, https://doi.org/10.1175/1520-0442(1996)009<3086:TROLLM>2.0.CO;2.

Jones, J. J., M. M. Bell, and P. J. Klotzbach, 2020: Tropical and subtropical North Atlantic vertical wind shear and seasonal tropical cyclone activity. *J. Climate*, **33**, 5413–5426, https://doi.org/10.1175/JCLI-D-19-0474.1.

Kaplan, J., and M. DeMaria, 2003: Large-scale characteristics of rapidly intensifying tropical cyclones in the North Atlantic Basin. *Wea. Forecasting*, **18**, 1093–1108, https://doi.org/10.1175/1520-0434(2003)018<1093:LCORIT>2.0.CO;2.

Karoly, D. J., 1983: Rossby wave propagation in a barotropic atmosphere. *Dyn. Atmos. Oceans*, **7**, 111–125, https://doi.org/10.1016/0377-0265(83)90013-1.

Kiladis, G. N., 1998: Observations of Rossby waves linked to convection over the eastern tropical Pacific. *J. Atmos. Sci.*, **55**, 321–339, https://doi.org/10.1175/1520-0469(1998)055<0321:OORWLT>2.0.CO;2.

——, and K. M. Weickmann, 1992: Circulation anomalies associated with tropical convection during northern winter. *Mon. Wea. Rev.*, **120**, 1900–1923, https://doi.org/10.1175/1520-0493(1992)120<1900:CAAWTC>2.0.CO;2.

Klotzbach, P. J., 2010: On the Madden–Julian oscillation–Atlantic hurricane relationship. *J. Climate*, **23**, 282–293, https://doi.org/10.1175/2009JCLI2978.1.

——, 2012: El Niño–Southern Oscillation, the Madden-Julian Oscillation and Atlantic Basin tropical cyclone rapid intensification. *J. Geophys. Res.*, **117**, D14104, https://doi.org/10.1029/2012JD017714.

——, 2014: The Madden–Julian Oscillation's impacts on worldwide tropical cyclone activity. *J. Climate*, **27**, 2317–2330, https://doi.org/10.1175/JCLI-D-13-00483.1.

——, and W. M. Gray, 2003: Forecasting September Atlantic basin tropical cyclone activity. *Wea. Forecasting*, **18**, 1109–1128,

https://doi.org/10.1175/1520-0434(2003)018<1109:FSABTC>2.0.CO;2.

——, and E. C. J. Oliver, 2015a: Variations in global tropical cyclone activity and the Madden-Julian Oscillation since the midtwentieth century. *Geophys. Res. Lett.*, **42**, 4199–4207, https://doi.org/10.1002/2015GL063966.

——, and ——, 2015b: Modulation of Atlantic basin tropical cyclone activity by the Madden–Julian oscillation (MJO) from 1905 to 2011. *J. Climate*, **28**, 204–217, https://doi.org/10.1175/JCLI-D-14-00509.1.

——, C. J. Schreck III, G. P. Compo, K. M. Wood, E. C. J. Oliver, S. G. Bowen, and M. M. Bell, 2023: Influence of the Madden-Julian Oscillation on continental United States hurricane landfalls. *Geophys. Res. Lett.*, **50**, e2023GL102762, https://doi.org/10.1029/2023GL102762.

Knippertz, P., and J. E. Martin, 2007: The role of dynamic and diabatic processes in the generation of cut-off lows over northwest Africa. *Meteor. Atmos. Phys.*, **96**, 3–19, https://doi.org/10.1007/s00703-006-0217-4.

Knutson, T. R., and K. M. Weickmann, 1987: 30–60 day atmospheric oscillations: Composite life cycles of convection and circulation anomalies. *Mon. Wea. Rev.*, **115**, 1407–1436, https://doi.org/10.1175/1520-0493(1987)115<1407:DAOCLC>2.0.CO;2.

Kobayashi, S., and Coauthors, 2015: The JRA-55 reanalysis: General specifications and basic characteristics. *J. Meteor. Soc. Japan*, **93**, 5–48, https://doi.org/10.2151/jmsj.2015-001.

Krishnamurti, T. N., D. K. Oosterhof, and A. V. Mehta, 1988: Air–sea interaction on the time scale of 30 to 50 days. *J. Atmos. Sci.*, **45**, 1304–1322, https://doi.org/10.1175/1520-0469(1988)045<1304:AIOTTS>2.0.CO;2.

Landsea, C. W., and J. L. Franklin, 2013: Atlantic hurricane database uncertainty and presentation of a new database format. *Mon. Wea. Rev.*, **141**, 3576–3592, https://doi.org/10.1175/MWR-D-12-00254.1.

Lau, K.-M., and L. Peno, 1992: Dynamics of atmospheric teleconnections during the northern summer. *J. Climate*, **5**, 140–158, https://doi.org/10.1175/1520-0442(1992)005<0140:DOATDT>2.0.CO;2.

——, and C.-H. Sui, 1997: Mechanisms of short-term sea surface temperature regulation: Observations during TOGA COARE. *J. Climate*, **10**, 465–472, https://doi.org/10.1175/1520-0442(1997)010<0465:MOSTSS>2.0.CO;2.

Lee, C.-Y., S. J. Camargo, F. Vitart, A. H. Sobel, and M. K. Tippett, 2018: Subseasonal tropical cyclone genesis prediction and MJO in the S2S dataset. *Wea. Forecasting*, **33**, 967–988, https://doi.org/10.1175/WAF-D-17-0165.1.

Lee, H.-J., and K.-H. Seo, 2019: Impact of the Madden-Julian Oscillation on Antarctic sea ice and its dynamical mechanism. *Sci. Rep.*, **9**, 10761, https://doi.org/10.1038/s41598-019-47150-3.

Leroy, A., and M. C. Wheeler, 2008: Statistical prediction of weekly tropical cyclone activity in the Southern Hemisphere. *Mon. Wea. Rev.*, **136**, 3637–3654, https://doi.org/10.1175/2008MWR2426.1.

Li, H., J. H. Richter, C.-Y. Lee, and H. Kim, 2022: Subseasonal tropical cyclone prediction and modulations by MJO and ENSO in CESM2. *J. Geophys. Res. Atmos.*, **127**, e2022JD036986, https://doi.org/10.1029/2022JD036986.

Li, R. K. K., T. Woollings, C. O'Reilly, and A. A. Scaife, 2020: Effect of the North Pacific tropospheric waveguide on the fidelity of model El Niño teleconnections. *J. Climate*, **33**, 5223–5237, https://doi.org/10.1175/JCLI-D-19-0156.1.

Li, W., Z. Wang, and M. S. Peng, 2016: Evaluating tropical cyclone forecasts from the NCEP Global Ensemble Forecasting System (GEFS) reforecast version 2. *Wea. Forecasting*, **31**, 895–916, https://doi.org/10.1175/WAF-D-15-0176.1.

——, ——, G. Zhang, M. S. Peng, S. G. Benjamin, and M. Zhao, 2018: Subseasonal variability of Rossby wave breaking and impacts on tropical cyclones during the North Atlantic warm season. *J. Climate*, **31**, 9679–9695, https://doi.org/10.1175/JCLI-D-17-0880.1.

Li, Y., J. Li, F. F. Jin, and S. Zhao, 2015: Interhemispheric propagation of stationary Rossby waves in a horizontally nonuniform background flow. *J. Atmos. Sci.*, **72**, 3233–3256, https://doi.org/10.1175/JAS-D-14-0239.1.

——, J. Feng, J. Li, and A. Hu, 2019: Equatorial windows and barriers for stationary Rossby wave propagation. *J. Climate*, **32**, 6117–6135, https://doi.org/10.1175/JCLI-D-18-0722.1.

Liebmann, B., and C. A. Smith, 1996: Description of complete (interpolated) outgoing longwave radiation data set. *Bull. Amer. Meteor. Soc.*, **77**, 1275–1277.

——, H. H. Hendon, and J. D. Glick, 1994: The relationship between tropical cyclones of the western Pacific and Indian Oceans and the Madden–Julian Oscillation. *J. Meteor. Soc. Japan*, **72**, 401–412, https://doi.org/10.2151/jmsj1965.72.3_401.

MacRitchie, K., and P. E. Roundy, 2016: The two-way relationship between the Madden–Julian Oscillation and anticyclonic wave breaking. *Quart. J. Roy. Meteor. Soc.*, **142**, 2159–2167, https://doi.org/10.1002/qj.2809.

Madden, R. A., and P. R. Julian, 1972: Description of global-scale circulation cells in the tropics with a 40–50 day period. *J. Atmos. Sci.*, **29**, 1109–1123, https://doi.org/10.1175/1520-0469(1972)029<1109:DOGSCC>2.0.CO;2.

Madonna, E., S. Limbach, C. Aebi, H. Joos, H. Wernli, and O. Martius, 2014: On the co-occurrence of warm conveyor belt outflows and PV streamers. *J. Atmos. Sci.*, **71**, 3668–3673, https://doi.org/10.1175/JAS-D-14-0119.1.

Maloney, E. D., and D. L. Hartmann, 2000: Modulation of hurricane activity in the Gulf of Mexico by the Madden–Julian Oscillation. *Science*, **287**, 2002–2004, https://doi.org/10.1126/science.287.5460.2002.

——, and J. T. Kiehl, 2002: MJO-related SST variations over the tropical eastern Pacific during Northern Hemisphere summer. *J. Climate*, **15**, 675–689, https://doi.org/10.1175/1520-0442(2002)015<0675:MRSVOT>2.0.CO;2.

——, and J. Shaman, 2008: Intraseasonal variability of the West African monsoon and Atlantic ITCZ. *J. Climate*, **21**, 2898–2918, https://doi.org/10.1175/2007JCLI1999.1.

Manganello, J. V., B. A. Cash, E. T. Swenson, and J. L. Kinter III, 2019: Assessment of climatology and predictability of mid-Atlantic tropical cyclone landfalls in a high-atmospheric-resolution seasonal prediction system. *Mon. Wea. Rev.*, **147**, 2901–2917, https://doi.org/10.1175/MWR-D-19-0107.1.

Matthews, A. J., B. J. Hoskins, and M. Masutani, 2004: The global response to tropical heating in the Madden-Julian oscillation during the northern winter. *Quart. J. Roy. Meteor. Soc.*, **130**, 1991–2011, https://doi.org/10.1256/qj.02.123.

McIntyre, M. E., and T. N. Palmer, 1983: Breaking planetary waves in the stratosphere. *Nature*, **305**, 593–600, https://doi.org/10.1038/305593a0.

Mo, K. C., 2000: The association between intraseasonal oscillations and tropical storms in the Atlantic Basin. *Mon. Wea. Rev.*, **128**, 4097–4107, https://doi.org/10.1175/1520-0493(2000)129<4097:TABIOA>2.0.CO;2.

Moore, R. W., O. Martius, and T. Spengler, 2010: The modulation of the subtropical and extratropical atmosphere in the Pacific basin in response to the Madden–Julian Oscillation. *Mon. Wea. Rev.*, **138**, 2761–2779, https://doi.org/10.1175/2010MWR3194.1.

Mori, M., and M. Watanabe, 2008: The growth and triggering mechanisms of the PNA: A MJO-PNA coherence. *J. Meteor. Soc. Japan*, **86**, 213–236, https://doi.org/10.2151/jmsj.86.213.

Moser, B. K., and G. R. Stevens, 1992: Homogeneity of variance in the two-sample means test. *Amer. Stat.*, **46**, 19–21, https://doi.org/10.1080/00031305.1992.10475839.

OFCM, 2023: National Hurricane Operations Plan. Office of the Federal Coordinator for Meteorological Services and Supporting Research Tech. Rep. FCM-P12-2023, 193 pp., https://www.weather.gov/media/nws/IHC2023/2023_nhop.pdf.

Papin, P. P., L. F. Bosart, and R. D. Torn, 2020: A feature-based approach to classifying summertime potential vorticity streamers linked to Rossby wave breaking in the North Atlantic Basin. *J. Climate*, **33**, 5953–5969, https://doi.org/10.1175/JCLI-D-19-0812.1.

——, Reynolds, C. A., and Janiga, M. A., 2023: Linkages between potential vorticity streamer activity and tropical cyclone predictability on subseasonal time scales. *Mon. Wea. Rev.*, **151**, 1005–1017, https://doi.org/10.1175/MWR-D-22-0038.1.

Postel, G. A., and M. H. Hitchman, 1999: A climatology of Rossby wave breaking along the subtropical tropopause. *J. Atmos. Sci.*, **56**, 359–373, https://doi.org/10.1175/1520-0469(1999)056<0359:ACORWB>2.0.CO;2.

——, and ——, 2001: A case study of Rossby wave breaking along the subtropical tropopause. *Mon. Wea. Rev.*, **129**, 2555–2569, https://doi.org/10.1175/1520-0493(2001)129<2555:ACSORW>2.0.CO;2.

Press, W. H., S. A. Teukolsky, W. T. Vetterling, and B. P. Flannery, 1992: Adaptive stepsize control for Runge-Kutta. *Numerical Recipes in Fortran 77: The Art of Scientific Computing*, L. Cowles and A. Harvey, Eds., Cambridge University Press, 704–708.

Randel, W. J., and I. M. Held, 1991: Phase speed spectra of transient eddy fluxes and critical layer absorption. *J. Atmos. Sci.*, **48**, 688–697, https://doi.org/10.1175/1520-0469(1991)048<0688:PSSOTE>2.0.CO;2.

Sakaguchi, K., J. Lu, L. R. Leung, C. Zhao, Y. Li, and S. Hagos, 2016: Sources and pathways of the upscale effects on the Southern Hemisphere jet in MPAS-CAM4 variable-resolution simulations. *J. Adv. Model. Earth Syst.*, **8**, 1786–1805, https://doi.org/10.1002/2016MS000743.

Salby, M. L., and H. H. Hendon, 1994: Intraseasonal behavior of clouds, temperature, and motion in the tropics. *J. Atmos. Sci.*, **51**, 2207–2224, https://doi.org/10.1175/1520-0469(1994)051<2207:IBOCTA>2.0.CO;2.

Sardeshmukh, P. D., and B. J. Hoskins, 1988: The generation of global rotational flow by steady idealized tropical divergence. *J. Atmos. Sci.*, **45**, 1228–1251, https://doi.org/10.1175/1520-0469(1988)045<1228:TGOGRF>2.0.CO;2.

Seo, K.-H., and S.-W. Son, 2012: The global atmospheric circulation response to tropical diabatic heating associated with the Madden–Julian oscillation during northern winter. *J. Atmos. Sci.*, **69**, 79–96, https://doi.org/10.1175/2011JAS3686.1.

——, and H.-J. Lee, 2017: Mechanisms for a PNA-like teleconnection pattern in response to the MJO. *J. Atmos. Sci.*, **74**, 1767–1781, https://doi.org/10.1175/JAS-D-16-0343.1.

Starr, V. P., 1948: An essay on the general circulation of the Earth's atmosphere. *J. Meteor.*, **5**, 39–43, https://doi.org/10.1175/1520-0469(1948)005<0039:AEOTGC>2.0.CO;2.

Strong, C., and G. Magnusdottir, 2008: Tropospheric Rossby wave breaking and the NAO/NAM. *J. Atmos. Sci.*, **65**, 2861–2876, https://doi.org/10.1175/2008JAS2632.1.

——, and ——, 2009: The role of tropospheric Rossby wave breaking in the Pacific decadal oscillation. *J. Climate*, **22**, 1819–1833, https://doi.org/10.1175/2008JCLI2593.1.

Subramanian, A., M. Jochum, A. J. Miller, R. Neale, H. Seo, D. Waliser, and R. Murtugudde, 2014: The MJO and global warming: A study in CCSM4. *Climate Dyn.*, **42**, 2019–2031, https://doi.org/10.1007/s00382-013-1846-1.

Swenson, E. T., and D. M. Straus, 2017: Rossby wave breaking and transient eddy forcing during Euro-Atlantic circulation regimes. *J. Atmos. Sci.*, **74**, 1735–1755, https://doi.org/10.1175/JAS-D-16-0263.1.

Thorncroft, C., and K. Hodges, 2001: African easterly wave variability and its relationship to Atlantic tropical cyclone activity. *J. Climate*, **14**, 1166–1179, https://doi.org/10.1175/1520-0442(2001)014<1166:AEWVAI>2.0.CO;2.

——, B. J. Hoskins, and M. E. McIntyre, 1993: Two paradigms of baroclinic-wave life-cycle behaviour. *Quart. J. Roy. Meteor. Soc.*, **119**, 17–55, https://doi.org/10.1002/qj.49711950903.

Trenberth, K. E., 1986: An assessment of the impact of transient eddies on the zonal flow during a blocking episode using localized Eliassen-Palm flux diagnostics. *J. Atmos. Sci.*, **43**, 2070–2087, https://doi.org/10.1175/1520-0469(1986)043<2070:AAOTIO>2.0.CO;2.

Tseng, K.-C., E. Maloney, and E. Barnes, 2019: The consistency of MJO teleconnection patterns: An explanation using linear Rossby wave theory. *J. Climate*, **32**, 531–548, https://doi.org/10.1175/JCLI-D-18-0211.1.

Ventrice, M. J., C. D. Thorncroft, and P. E. Roundy, 2011: The Madden–Julian Oscillation's influence on African easterly waves and downstream tropical cyclogenesis. *Mon. Wea. Rev.*, **139**, 2704–2722, https://doi.org/10.1175/MWR-D-10-05028.1.

Vitart, F., 2009: Impact of the Madden Julian Oscillation on tropical storms and risk of landfall in the ECMWF forecast system. *Geophys. Res. Lett.*, **36**, L15802, https://doi.org/10.1029/2009GL039089.

——, A. Leroy, and M. C. Wheeler, 2010: A comparison of dynamical and statistical predictions of weekly tropical cyclone activity in the Southern Hemisphere. *Mon. Wea. Rev.*, **138**, 3671–3682, https://doi.org/10.1175/2010MWR3343.1.

Wang, B., and T. Li, 1994: Convective interaction with boundary-layer dynamics in the development of a tropical intraseasonal system. *J. Atmos. Sci.*, **51**, 1386–1400, https://doi.org/10.1175/1520-0469(1994)051<1386:CIWBLD>2.0.CO;2.

Wang, C., and D. B. Enfield, 2001: The tropical Western Hemisphere warm pool. *Geophys. Res. Lett.*, **28**, 1635–1638, https://doi.org/10.1029/2000GL011763.

——, and ——, 2003: A further study of the tropical Western Hemisphere warm pool. *J. Climate*, **16**, 1476–1493, https://doi.org/10.1175/1520-0442(2003)016%3C1476:AFSOTT%3E2.0.CO;2.

Wang, F., W. Tian, F. Xie, J. Zhang, and Y. Han, 2018: Effect of Madden–Julian Oscillation occurrence frequency on the interannual variability of Northern Hemisphere stratospheric wave activity in winter. *J. Climate*, **31**, 5031–5049, https://doi.org/10.1175/JCLI-D-17-0476.1.

Wang, J., H. Kim, D. Kim, S. A. Henderson, C. Stan, and E. D. Maloney, 2020: MJO teleconnections over the PNA region in climate models. Part II: Impacts of the MJO and basic state. *J. Climate*, **33**, 5081–5101, https://doi.org/10.1175/JCLI-D-19-0865.1.

Wang, T., and T. Li, 2021: Factors controlling the diversities of MJO propagation and intensity. *J. Climate*, **34**, 6549–6563, https://doi.org/10.1175/JCLI-D-20-0859.1.

Waugh, D. W., 2005: Impact of potential vorticity intrusions on subtropical upper tropospheric humidity. *J. Geophys. Res.*, **110**, D11305, https://doi.org/10.1029/2004JD005664.

——, and L. M. Polvani, 2000: Climatology of intrusions into the tropical upper troposphere. *Geophys. Res. Lett.*, **27**, 3857–3860, https://doi.org/10.1029/2000GL012250.

Wheeler, M. C., and H. H. Hendon, 2004: An all-season real-time multivariate MJO index: Development of an index for monitoring and prediction. *Mon. Wea. Rev.*, **132**, 1917–1932, https://doi.org/10.1175/1520-0493(2004)132<1917:AARMMI>2.0.CO;2.

Woollings, T., B. Hoskins, M. Blackburn, and P. Berrisford, 2008: A new Rossby wave–breaking interpretation of the North Atlantic Oscillation. *J. Atmos. Sci.*, **65**, 609–626, https://doi.org/10.1175/2007JAS2347.1.

Xie, Y.-B., S.-J. Chen, I.-L. Zhang, and Y.-L. Hung, 1963: A preliminarily statistic and synoptic study about the basic currents over southeastern Asia and the initiation of typhoon (in Chinese). *Acta Meteor. Sin.*, **33**, 206–217, https://doi.org/10.11676/qxxb1963.020.

Zavadoff, B. L., and B. P. Kirtman, 2019: North Atlantic summertime anticyclonic Rossby wave breaking: Climatology, impacts, and connections to the Pacific decadal oscillation. *J. Climate*, **32**, 485–500, https://doi.org/10.1175/JCLI-D-18-0304.1.

——, and ——, 2021: The Pacific decadal oscillation as a modulator of summertime North Atlantic Rossby wave breaking. *Climate Dyn.*, **56**, 207–225, https://doi.org/10.1007/s00382-020-05475-0.

Zhang, C., 1996: Atmospheric intraseasonal variability at the surface in the tropical western Pacific Ocean. *J. Atmos. Sci.*, **53**, 739–758, https://doi.org/10.1175/1520-0469(1996)053<0739:AIVATS>2.0.CO;2.

——, 2005: Madden-Julian Oscillation. *Rev. Geophys.*, **43**, RG2003, https://doi.org/10.1029/2004RG000158.

——, 2013: Madden–Julian Oscillation: Bridging weather and climate. *Bull. Amer. Meteor. Soc.*, **94**, 1849–1870, https://doi.org/10.1175/BAMS-D-12-00026.1.

——, and M. Dong, 2004: Seasonality in the Madden–Julian Oscillation. *J. Climate*, **17**, 3169–3180, https://doi.org/10.1175/1520-0442(2004)017<3169:SITMO>2.0.CO;2.

Zhang, G., and Z. Wang, 2018: North Atlantic extratropical Rossby wave breaking during the warm season: Wave life cycle and role of diabatic heating. *Mon. Wea. Rev.*, **146**, 695–712, https://doi.org/10.1175/MWR-D-17-0204.1.

——, and ——, 2019: North Atlantic Rossby wave breaking during the hurricane season: Association with tropical and extratropical variability. *J. Climate*, **32**, 3777–3801, https://doi.org/10.1175/JCLI-D-18-0299.1.

——, ——, T. J. Dunkerton, M. S. Peng, and G. Magnusdottir, 2016: Extratropical impacts on Atlantic tropical cyclone activity. *J. Atmos. Sci.*, **73**, 1401–1418, https://doi.org/10.1175/JAS-D-15-0154.1.

——, ——, M. S. Peng, and G. Magnusdottir, 2017: Characteristics and impacts of extratropical Rossby wave breaking

during the Atlantic hurricane season. *J. Climate*, **30**, 2363–2379, https://doi.org/10.1175/JCLI-D-16-0425.1.

Zhao, S., J. Li, and Y. Li, 2015: Dynamics of an interhemispheric teleconnection across the critical latitude through a southerly duct during boreal winter. *J. Climate*, **28**, 7437–7456, https://doi.org/10.1175/JCLI-D-14-00425.1.

——, ——, ——, F.-F. Jin, and J. Zheng, 2019: Interhemispheric influence of Indo-Pacific convection oscillation on Southern Hemisphere rainfall through southward propagation of Rossby waves. *Climate Dyn.*, **52**, 3203–3221, https://doi.org/10.1007/s00382-018-4324-y.

Zhou, S., M. L'Heureux, S. Weaver, and A. Kumar, 2012: A composite study of the MJO influence on the surface air temperature and precipitation over the continental United States. *Climate Dyn.*, **38**, 1459–1471, https://doi.org/10.1007/s00382-011-1001-9.